


Complex Cloud-Sea Background Simulation for Space-Based Infrared Payload Digital Twin

Wen Sun , Yejin Li , Fenghong Li , Guangsen Liu , and Peng Rao , *Member, IEEE*

Abstract—The advent of Industry 4.0 has highlighted the requirements for the digitization and intelligent evolution of space-based payloads. To address challenges like limited data samples and simulate infrared images in various scenarios, this study proposes a hybrid data-driven and fractal-driven cloud-sea scenario simulation approach for high-precision infrared images at space-based detection scales. Static cloud-sea scenes are generated using Qilu-2 and New Technology satellite images, while dynamic scenarios are simulated with our iterative fractal dimension optimization algorithm. Next, we propose a high-precision infrared cloud-sea simulation method based on these simulate scenarios. Finally, we validate the confidence of the simulated images through morphological assessment using a 2-D histogram and radiative accuracy evaluation based on Moderate resolution atmospheric transmission (MODTRAN) results. Experimental results confirm the method’s accuracy, showing close alignment with on-orbit images. In the 2.7–3.0 μm band, our average radiance is consistent with MODTRAN. Specifically, for reflection angles below 60° , the root mean square error between our results and MODTRAN results is about 12.3% in the 3.0–5.0 μm band, and around 3.7% in the 8.0–14.0 μm band. Morphological assessment shows an average error of about 8.3% when compared to on-orbit images. This method allows for generating multiband, multispecies, and multiscale complex cloud-sea scenario images for digital infrared payloads with high flexibility and confidence.

Index Terms—Cloud-sea scenario, data-driven, digital twin, fractal-driven, infrared radiation, space-based infrared payloads.

I. INTRODUCTION

WITH the advent of Industry 4.0, the demand for the digitalization and intelligent development of aerospace payloads has increased [1]. High-precision detection backgrounds are essential inputs for digital payloads and determine the overall performance of these payloads. To construct a digital detection background model and address the challenges posed by “small sample” and “zero sample” infrared background images, this study simulates multitemporal, multiparameter, and multimode

infrared images observed by infrared payloads in multidomain scenarios. The findings of this study can provide technical support for digital payload research, which is critical for enhancing the performance of next-generation infrared payloads in target detection, recognition, and tracking.

Given that the average global annual cloud cover is approximately 66% [2], cloud-sea scenarios represent a primary environmental factor for space-based infrared payloads. Simulating these scenarios provides complex observational data that improves simulation accuracy, thus supporting comprehensive performance evaluation and optimization. Moreover, these data enhance intelligent detection algorithms, improving their robustness across operational contexts. Therefore, cloud-sea scenario simulation is integral to high-fidelity digital twin systems and essential for advancing space-based infrared payload performance.

Currently, although single-scene simulation technologies for clouds and oceans are relatively advanced [3], [4], [5], [6], [7], there are independent studies on infrared radiation from cloud layers and sea surfaces [8], [9], [10], [11], [12], [13], [14], [15], these methods are overly simplistic and inadequate for the detection requirements of space-based infrared payloads. Furthermore, while recent AI-based approaches have shown promise in infrared image simulation [16], [17], [18], [19], they are constrained by limited training data and often fail to generate images with accurate physical properties. For the detection requirements of space-based infrared payloads, thus rendering them insufficient for practical applications.

- 1) Most existing infrared simulation systems are primarily designed for ground-based observation scenarios and typically rely on simplified empirical models, thus lacking the ability to simulate complex scenes.
- 2) There is a lack of space-based detection scale infrared cloud-sea scene simulation technology with 100-m resolution, failing to meet high-precision requirements.
- 3) AI-based deep learning methods for infrared image generation are constrained by insufficient training data and inability to produce images with precise physical significance, making them inadequate for quantitative analysis and physical property studies.
- 4) This technological gap limits the capacity for high-accuracy simulations under complex observational conditions, which hinders effective support for the performance evaluation and optimization of digital twin systems for space-based infrared payloads.

This study addresses the limitations of existing infrared cloud-sea detection background models by meeting the digital

Received 27 August 2024; revised 28 November 2024; accepted 23 December 2024. Date of publication 27 December 2024; date of current version 10 January 2025. (Corresponding author: Peng Rao.)

Wen Sun, Fenghong Li, and Guangsen Liu are with the Key Laboratory of Intelligent Infrared Perception, Chinese Academy of Sciences, Shanghai 200083, China, also with the Shanghai Institute of Technical Physics, Chinese Academy of Sciences, Shanghai 200083, China, and also with the University of Chinese Academy of Sciences, Beijing 100049, China (e-mail: sunwen21@mails.ucas.ac.cn; lifenghong21@mails.ucas.ac.cn; liuguangsen20@mails.ucas.ac.cn).

Yejin Li and Peng Rao are with the Key Laboratory of Intelligent Infrared Perception, Chinese Academy of Sciences, Shanghai 200083, China, and also with Shanghai Institute of Technical Physics, Chinese Academy of Sciences, Shanghai 200083, China (e-mail: yejinli@mail.sitp.ac.cn; peng_rao@mail.sitp.ac.cn).

Digital Object Identifier 10.1109/JSTARS.2024.3523395

requirements of infrared payloads. We propose a hybrid data-driven and fractal-driven cloud-sea scenario simulation (HCSS) algorithm that leverages real on-orbit satellite images to simulate static cloud-sea scenes. For dynamic simulations, a fractal algorithm is optimized using a dynamic iterative approach based on fractal dimension (FD). In the optical properties calculation module, the Mie scattering theory and Cox–Munk model are utilized to compute the optical parameters of the cloud-sea scenes. By comprehensively considering all radiation sources, a high-precision infrared cloud-sea radiation calculation model is developed, enabling realistic infrared cloud-sea image simulations. In addition, the morphological accuracy of the simulated images is assessed using a 2-D histogram-based confidence evaluation, while the radiative accuracy is validated through comparison with Moderate resolution atmospheric transmission (MODTRAN) calculations. Our contributions can be summarized as follows:

- 1) We propose a HCSS algorithm capable of generating multiscenario, multiscale, and multicoverage high-confidence complex infrared cloud-sea images.
- 2) A comprehensive cloud-sea infrared radiation calculation model is developed, providing multitemporal, multiband, and multitype complex infrared background radiation data.
- 3) High-confidence cloud-sea images are generated with radiation calculation results that exhibited close alignment with MODTRAN results, and the average root mean square error (RMSE) for morphological accuracy is approximately 8.3%.
- 4) The resulting infrared radiation model serves as an input for digital payload prototypes, enabling more efficient testing and optimization of on-orbit systems.

II. RELATED WORKS

Traditional research on cloud-sea simulations typically addresses cloud and sea surface simulations and infrared radiation characteristics in isolation. Two main methods for generating the sea surface fluctuation are numerical modeling [3], [4], [6] and physical simulation [5]. The aim of physical simulations is to solve wave equations, which are significantly complex, to obtain analytical solutions [5]. The advantage of numerical modeling is that it can adapt to various sea conditions, spatial resolutions, and detection ranges without physical experiments or actual measurements, e.g., the Pierson–Moskowitz (P-M) spectrum [3] and the Joint North Sea Wave Project (JONSWAP) spectrum [4], [6]. Moreover, cloud scenario generation can currently be divided into three methods [7].

- 1) Data-driven methods: Utilizing measured data is the simplest method for simulating clouds, which involves spectral transformation, resolution transformation, and cloud feature extraction [20], [21], [22], [23], [24]. Techniques based on neural networks and deep learning are employed to generate cloud images [25], [26]. The advantage of this approach is that the simulation can be readily validated with authentic data. However, it is limited by the availability of data, thus making it challenging to cover all regions and climatic conditions.

- 2) Physics-driven methods: Using partial differential equations to solve the fluid model of clouds can achieve realistic simulation effects based on different parameters and initial environmental conditions [27], [28], [29]. However, employing fluid dynamics methods to simulate clouds is computationally complex, and this approach exhibits a low real-time performance.
- 3) Rule-based heuristic-driven methods: Such methods use simplified processes and computations to simulate clouds, thus making them straightforward and less computational intensive than physics-driven methods. The stochastic fractal theory is most frequently employed in heuristic-driven cloud simulation, typically based on the fast Fourier transform (FFT) method [30], [31]. Proposed multifractal algorithms subsequently describe clouds more accurately [10], [32], [33], [34], [35]. These algorithms can flexibly simulate cloud layers' features under specific weather conditions. However, they require strict parameter control, and unreasonable settings can result in low confidence.

The accuracy of infrared cloud and sea image simulation is critical for effective target detection and recognition in complex environments. Atmospheric radiative transfer models are critical for simulating radiative characteristics under such conditions, especially where cloud and aerosol interactions over dynamic sea surfaces are involved. Low-resolution transmission (LOWTRAN), a simplified model assuming a uniform atmosphere, is suitable for basic applications [36]. A thermal emission spectrometer (TES) provides rapid mid-wave infrared (MWIR) transmission estimates, which are critical for remote sensing [37]. An atmospheric radiative transfer simulator handles complex atmospheric conditions, including cloud and aerosol effects on MWIR radiation [38]. Discrete ordinates radiative transfer is commonly used for modeling scattering and absorption in horizontally layered atmospheres, although it can be computationally intensive [39]. Rapid radiative transfer model for television infrared observation satellite (TIROS) operational vertical sounder (TOVS) radiative transfer for TOVS (RTTOV) provides fast MWIR radiative transfer calculations, mainly for weather forecasting [40]. MODTRAN, which is known for its higher spectral resolution and capability to simulate complex atmospheric variations, effectively models radiative transfer phenomena. However, it is limited to providing numerical simulation results. It cannot generate 2-D cloud and sea scene simulation data [41].

In recent years, several representative infrared simulation systems, including IRMA [42], SSW [43], SIMSA [44], Vega/Vega Prim [45], CAMEO-SIM [46], and SE-Workbench-EO [47], etc., have been developed to simulate complex infrared scenarios, as shown in Fig. 1. However, all these systems are ground-based detection systems and the modules in these systems are relatively simplified. The most common methods are qualitative modeling simulations or semiempirical physical models, where empirical value selection introduces a subjective factor. There are cases wherein 3-D modeling software is used to generate 3-D scenes, followed by the generation of infrared scenes using physics-based modeling [14], [21], [48], [49], [50]. However, most of these tools are proprietary and costly, thus

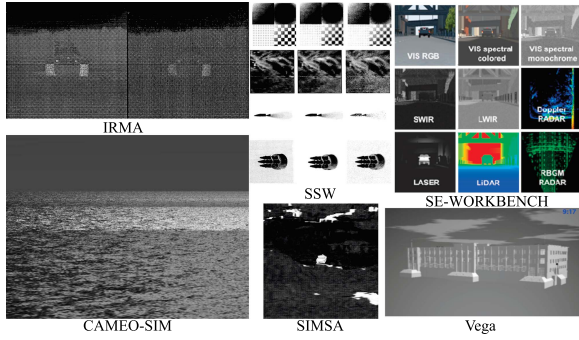


Fig. 1. Simulation results of the typical infrared systems.

posing accessibility challenges for general users. A common issue arises when simulating the physical effects of cloud-sea scenarios in that there are significant differences between the simulated degraded and real images. This discrepancy makes it difficult to establish a correspondence between on-orbit payloads and laboratory digital payloads, thus leading to challenges in accurately evaluating the system performance of on-orbit payloads.

In recent years, the rapid advancement of artificial intelligence (AI) in geosciences has significantly improved the simulation and comprehension of complex Earth systems [51]. Data-driven methods, especially deep learning (DL), provide prospective avenues for infrared image simulation. In particular, CycleGAN [17], [18] and Pix2Pix GAN Generative adversarial network (GAN) [19] are favored for their applications in domain adaptation and image translation, thus transforming visible light images into infrared representations. ThermalGAN [52] converts red, green, and blue (RGB) images to long-wave infrared (LWIR) images for person reidentification by predicting thermal segmentation maps and local temperature contrasts with two GANs, which are combined to generate the final thermal image. Özkanoğlu et al. [53] developed InfraGAN, which is a UNet-based network that learns the mapping between infrared and RGB image data, thus enabling the pixelwise classification of generated images. Li et al. [54] introduced a dual attention GAN (DAGAN) that enhances thermal image translation by separating and focusing on foreground and background features. For direct infrared image generation, Zhang et al. [55] developed SIR-GAN to enhance synthetic infrared images by learning bidirectional mappings between real and simulated domains. They constructed 3-D geometric models, applied physical modeling for infrared textures, and used OGRE rendering and atmospheric models to generate initial infrared images, which were then refined by SIR-GAN. The unique features of infrared scenes complexify the learning process, as a single generator cannot model all relevant characteristics simultaneously. Generating realistic infrared images from RGB data remains challenging. In addition, multiple deep learning models lack physical constraints, and the limited availability of labeled data hinders training, thus resulting in insufficient variation in target angles, time, and seasons. Acquiring large volumes of real remote sensing images is costly and requires extensive fieldwork and postprocessing.

III. MATERIALS AND METHODS

This study proposes a HCSS method focused on simulating complex infrared cloud-sea background images, as shown in Fig. 2. The process begins by identifying key scenario parameters, including atmospheric type, cloud type, sea conditions, observation geometry, time and location, and infrared band. For static scenarios, we employ a data-driven method using on-orbit images from the Qilu-2 and New Technology Satellites. For dynamic scenarios, we develop and optimize a fractal-driven method based on the FD of real clouds. Next, we analyze the optical properties of the cloud and sea using Mie scattering theory and the Cox–Munk model, integrating cloud and sea optical properties. These properties are then used to compute infrared radiation, considering factors such as self-radiation, reflection, path radiation, and total radiation. The resulting data are synthesized into simulated infrared images. Finally, we evaluate simulation confidence using 2-D histogram-based morphological analysis and validate the radiative simulation accuracy through comparison with MODTRAN.

A. Hybrid Data-Driven and Fractal-Driven Cloud-Sea Scenario Simulation

1) *Static Cloud-Sea Simulation based on the Data-Driven Method:* Infrared detection systems rely on image sequences derived from temperature differences in radiation between targets and their backgrounds for effective target detection, recognition, and tracking. Thus, in space-based infrared payload digital twin technology, one of the most critical and challenging tasks is accurately simulating infrared radiation characteristics in complex backgrounds. In digital twin models for space-based infrared payloads, cloud-sea scenarios represent detection backgrounds where clouds act as primary targets against an oceanic background. Traditional static cloud simulations are constrained by the limitations of infrared cloud imagery. To address this, data from the Qilu-2 and New Technology satellites were utilized, with adaptive threshold processing, mask detection, and grayscale value extraction applied to generate realistic cloud images. The integration of these multisource datasets overcomes traditional limitations and significantly enhances the accuracy of cloud morphology, thus establishing a more reliable foundation for infrared simulation and improving overall simulation quality. In addition, an on-orbit cloud image database was developed, which contains comprehensive observational cloud data.

The 2-D simulation of the sea surface in these scenarios is effectively rendered using the P-M spectrum [3], which can be expressed as follows. The Pierson-Moskowitz spectrum with different wind speeds is illustrated in Fig. 3.

$$S(\omega) = \alpha \frac{g^2}{\omega^5} \exp \left[-\beta \left(\frac{g}{U\omega} \right)^4 \right] \quad (1)$$

where $\alpha = 8.1 \times 10^{-3}$, $\beta = 0.74$, $g = 9.81$ m/s, ω represents the frequency, and U represents the wind speed, indicating the growth condition of the waves [46].

To simulate a cloud-sea scenario, when the static scenes of clouds and the sea are modeled, the cloud layer is overlaid onto the sea surface, with the composite image adjusted to match

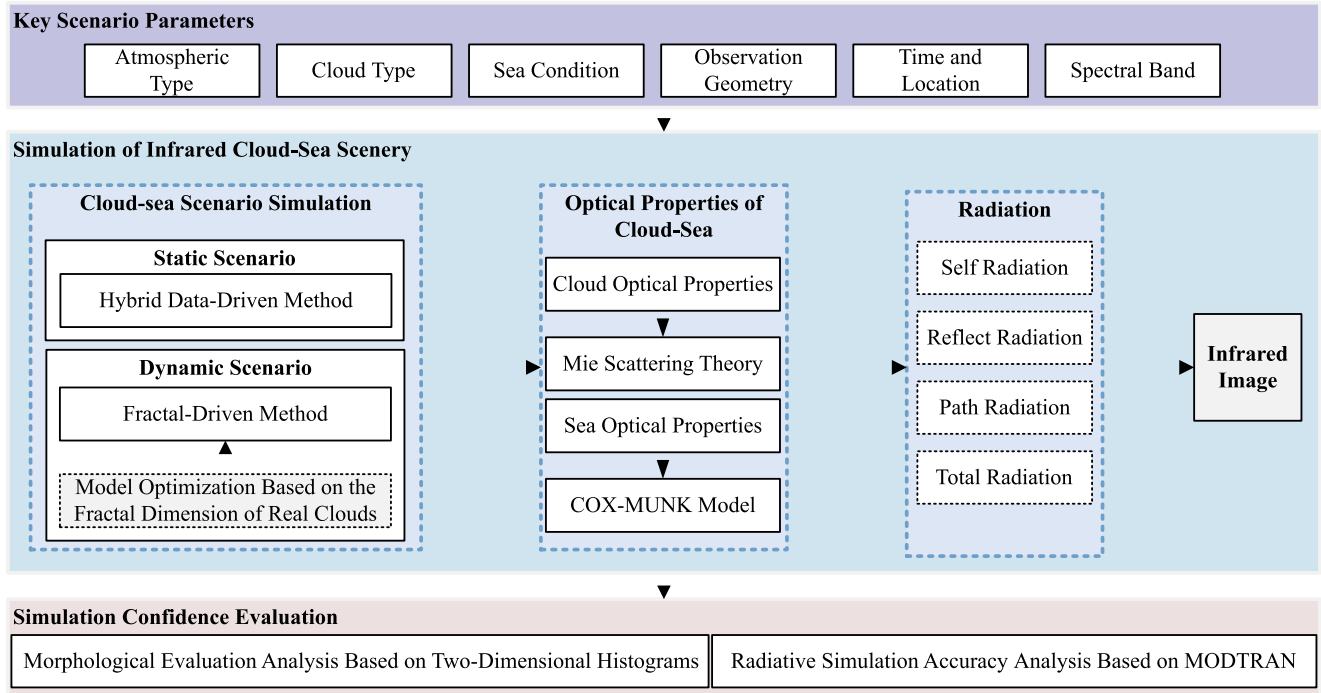


Fig. 2. Flowchart of our proposed method.

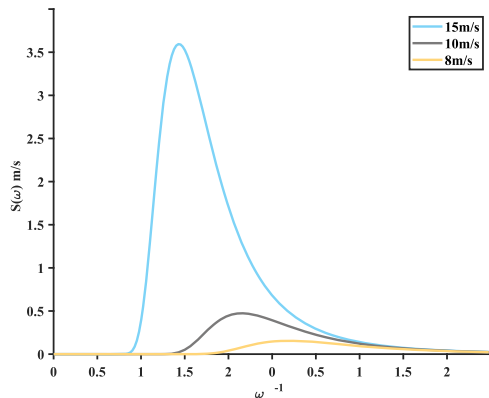


Fig. 3. Pierson–Moskowitz spectrum with different wind speeds.

the spatial resolution and field of view of space-based infrared sensors. This process produces a realistic cloud-sea scene from a space-based detection perspective, thus facilitating accurate performance modeling and the evaluation of digital infrared payload detection systems.

2) *Dynamic Cloud-Sea Simulation via the Fractal-Driven Method*: In space-based infrared payload detection, the cloud-sea background is a key environment, especially for long-term observation of high-speed targets. Simulating dynamic cloud-sea scenarios is critical for digital development, as it aids in optimizing payload parameters, thus reducing costs and risks, and in assessing detection performance across varying backgrounds. In addition, these simulations support research related to cloud layer effects on infrared transmission and

contribute to building a comprehensive background feature database.

This study presents a novel cloud-sea scene modeling method based on a fractal-driven approach. Centered on the optimization of FD derived from on-orbit images, the method establishes a multiscale, multitype framework for simulating cloud-sea morphology, thus significantly enhancing the realism and accuracy of cloud-sea scene simulations. As detailed in this study, first, the dynamic model of the cloud field was established based on fractal theory, where A_n is an n -dimensional random matrix following a zero-mean Gaussian distribution, the real function $S_n(x)$ is the interpolation function of A_n at the coordinate point X , the interpolation method is the cubic interpolation, and V_n is an n -dimensional position vector. The random function is defined as follows:

$$V_n(X) = \sum_{k=k_0}^{k_{\max}} \frac{1}{\gamma^{kH}} S_n \left(\gamma^k \frac{X}{L} \right) \quad (2)$$

where γ is the gap parameter, which influences the richness of image details; in general, values of 2, 3, or 4 suffice to meet human visual perception requirements. H is the Hurst parameter. A higher H value increases the low-frequency components, thus resulting in a smoother image, whereas a lower H value adds more detail. Typically, $0 < H < 1$. L is the interpolation resolution, where $L = (l_1, l_2, \dots, l_n)$ is an n -dimensional matrix used to calculate the interpolated positions of X in matrix A_n , which determines the density of interpolated data points adjacent to A_n . Moreover, k is the summation term, with k_0 and k_{\max} representing the lower and upper limits of the summation term, respectively. Different

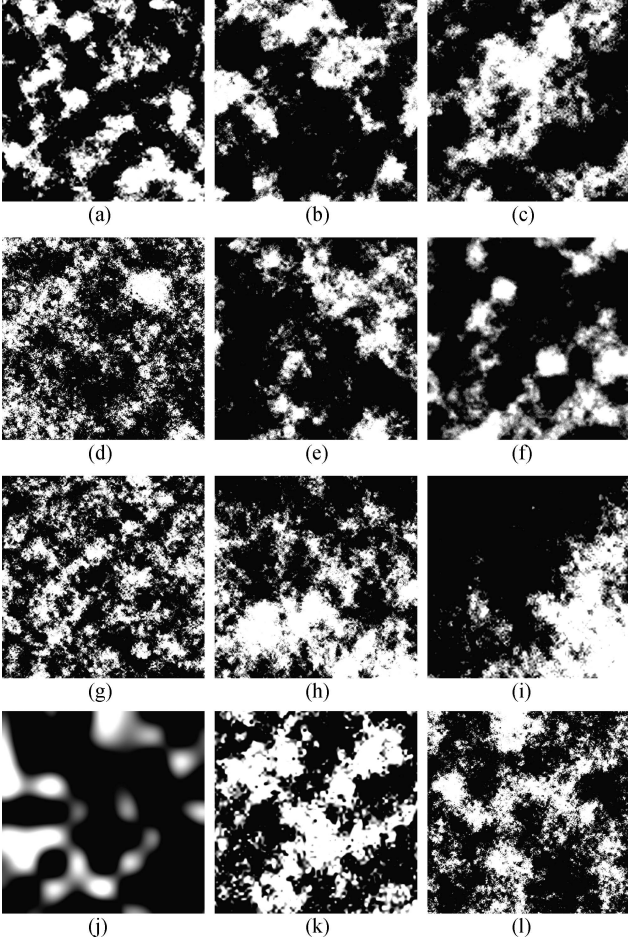


Fig. 4. Fractal images with different parameter settings. (a) $r = 2$. (b) $r = 3$. (c) $r = 4$. (d) $H = 0.1$. (e) $H = 0.5$. (f) $H = 0.8$. (g) $L = [5, 5]$. (h) $L = [20, 20]$. (i) $L = [50, 50]$. (j) $k_{max} = 0$. (k) $k_{max} = 2$. (l) $k_{max} = 4$.

parameter settings produce different effects, as illustrated in Fig. 4.

By extending (2) to four dimensions and fractalizing in the time dimension, a simulation of a 4-D dynamic cloud can be obtained as follows:

$$V_4(X(x, y, z, t)) = \sum_{k=k_0}^{\infty} \frac{1}{\gamma^{kH}} S_4 \left(\gamma^k \frac{X(x, y, z, t)}{L(x, y, z, t)} \right). \quad (3)$$

To further simulate the impact of air convection on the overall position of clouds, we introduce the influence of time t in the x and y dimensions. We assumed that the cloud layer moves horizontally with $v = (v_x, v_y)$, where v_x and v_y represent the velocity components in the x and y directions, respectively. Equation (3) can be updated as follows:

$$V_4(X(x + v_x, y + v_y, z, t)) = \sum_{k=k_0}^{k_{max}} \frac{1}{\gamma^{kH}} \cdot S_4 \left(\gamma^k \frac{X(x + v_x, y + v_y, z, t)}{L(x, y, z, t)} \right). \quad (4)$$

Algorithm 1: Dynamic Cloud Simulation With Iterative FD Optimization.

Input: Cloud type, cloud cover, image size, on-orbit image FD range

Output: Fractal dynamic cloud images

- 1: Initialize the cloud type, cloud cover, image size, and fractal control parameters.
 - 2: Generate dynamic clouds based on the fractal algorithm.
 - 3: Calculate the initial FD of the dynamic clouds.
 - 4: **while** FD is not within the on-orbit image FD range **do**
 - 5: Adjust the fractal control parameters.
 - 6: Generate new dynamic clouds using the updated fractal parameters.
 - 7: Recalculate the FD of the optimized fractal dynamic cloud images.
 - 8: **end while**
 - 9: **return** the optimized fractal dynamic cloud images.
-

After performing fractal interpolation based on (4), the matrix followed a Gaussian random distribution with a mean of 0, a standard deviation of 1, and values ranging from -5 to 5 . The error function was then used to transform this random matrix V_n into a uniform distribution between 0 and 1, which facilitated the subsequent division of cloud and cloud-free regions

$$p = \frac{1}{2} \left(1 + \operatorname{erf} \left(\frac{V_n}{\sqrt{2}} \right) \right). \quad (5)$$

Here erf is the error function, and p represents the uniformly transformed cloud fraction value. Thereafter, sort the matrix p based on the specified cloud coverage rate. Areas with coverage below the threshold are classified as cloud-free, which is denoted as $C(x, y) = 0$, whereas regions exceeding the threshold are considered cloud-covered, and represented by $C(x, y) \neq 0$ [56].

To enhance the credibility of the simulated clouds, a method based on iterative optimization of the FD derived from on-orbit imagery was proposed to model dynamic cloud morphology. This approach first calculates the FD of clouds extracted from on-orbit images, verifies the range of FD for the simulated clouds, and iteratively adjusts the fractal control parameters. This process enhances the credibility and accuracy of the simulated cloud images. The FD of the graphics can be calculated using

$$FD = \lim_{\epsilon \rightarrow \infty} \frac{\log_N \epsilon}{\log(1/\epsilon)} \quad (6)$$

where ϵ represents the unit of measurement. The measurement method uses the measurement unit to cover the measured object, where N represents the number of the measurement unit used to cover a fractal object [57], [58].

For cloud-covered regions, thickness mapping is performed using a fractal 2-D matrix based on the cloud-base and cloud-top heights. The mapping from the cloud brightness distribution

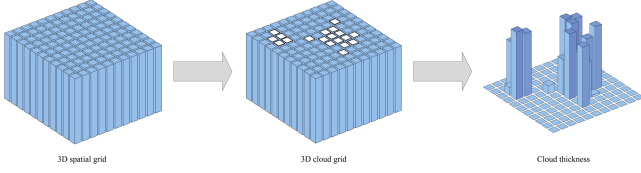


Fig. 5. 3-D spatial morphology modeling of clouds.

matrix to the cloud thickness matrix is approximately linear. Assuming the cloud thickness distribution ranges from Th_{\min} to Th_{\max} , the cloud thickness value Th in the cloud-covered region can be mapped, as shown in (7). When $C(x, y) = 0$, $Th(x, y)$ was set to 0, as illustrated in Fig. 5

$$Th(x, y) = Th_{\min} + \Delta Th \frac{C(x, y) - C_{\min}}{C_{\max} - C_{\min}}. \quad (7)$$

In space-based observation scenarios, the limited spatial resolution of satellite sensors makes it challenging to accurately capture subtle variations on the sea surface. From a top-down perspective, microfeatures such as waves and ripples on the sea surface are generally of scales smaller than the resolution capability of the sensors. Consequently, these details are averaged out during the imaging process, thus rendering the sea surface as a relatively homogeneous, large-area region. This characteristic simplifies the modeling of the sea surface background. In the simulation of dynamic cloud-sea scenes, a P-M-based approach was employed to simulate the sea surface. In contrast, subsequent infrared scene simulations are more focused on the sea surface infrared optical properties, primarily considering emissivity and reflectivity to ensure accurate calculations of sea surface radiation. Therefore, dynamic cloud-sea simulation scenarios are proposed.

B. Calculation of Optical Properties of Cloud and Sea.

In space-based satellite observation scenarios, high-altitude cirrus clouds are commonly observed. These clouds, which are typically located above 6 km, are cold and primarily composed of ice crystals; thus, they are referred to as ice clouds. In contrast, clouds with lower cloud-top heights are generally composed of water particles. The significant difference in optical properties between ice clouds and water clouds significantly influences radiative calculations. Therefore, in this study, we categorized clouds into two types, i.e., ice clouds and water clouds, for radiative computations. The particle size within clouds is comparable to the wavelength of infrared radiation, thus making Mie scattering the primary interaction between clouds and infrared radiation. By calculating the extinction efficiency, scattering efficiency, absorption efficiency, single-scattering albedo and phase function based on Mie scattering theory, the cloud emissivity and reflectivity can be obtained, which serve as a basis for subsequent radiative calculations [59].

The calculation formula for the infrared emissivity of clouds ϵ_{cloud} is expressed as follows:

$$\epsilon_{\text{cloud}} = 1 - \exp(-K_{\text{abs}}z) \quad (8)$$

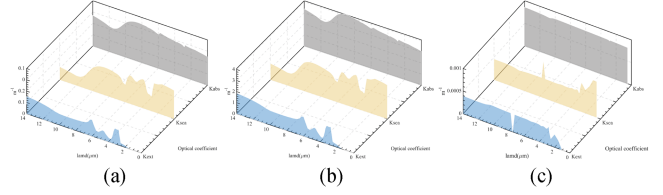


Fig. 6. Optical property parameters of clouds in the 0–14.0 μm band: (a) cumulus (water cloud), (b) stratus (water cloud), and (c) cirrus (ice cloud).

where K_{abs} is the absorption coefficient of the clouds, and z is the optical thickness of the clouds. The definition of the absorption coefficient varies under different circumstances. For water clouds, the expression is as follows:

$$K_{\text{abswatercloud}}(\lambda) = \pi \int_{r_1}^{r_2} r^2 Q_{\text{abs}}(\lambda, r) n(r) dr \quad (9)$$

where r represents the radius of the cloud droplets, $n(r)$ is the size distribution function of the clouds, $(r) = ar^\alpha e^{-\beta r^v}$, α is the particle number density, and β and v are morphological parameters, which are empirical coefficients based on statistical observation data [60]. Moreover, $Q_{\text{abs}}(\lambda, r)$ is the absorption efficiency of clouds with a wavelength λ and radius r , which can be calculated through Mie scattering theory [61]. The absorption coefficient for ice clouds is expressed as

$$k_{\text{absicecloud}}(\lambda) = (1 - w_0) Q_{\text{ext}} \quad (10)$$

where $Q_{\text{ext}}(\lambda, r)$ is the extinction coefficient of clouds with a wavelength λ and radius of r . The results of the optical properties of the cloud for 0–14 μm are shown in Fig. 6.

w_0 is the single-scattering albedo, which can be expressed as follows:

$$w_0 = \frac{Q_{\text{sca}}}{Q_{\text{ext}}}. \quad (11)$$

As presented below, $BRDF(\lambda, \theta_i, \varphi_i, \theta_r, \varphi_r)$ is the bidirectional reflectance distribution function (BRDF) of the cloud

$$BRDF(\lambda, \theta_i, \varphi_i, \theta_r, \varphi_r) = \frac{w_0}{4\pi} P(\theta) \frac{\cos \theta_i}{\cos \theta_i + \cos \theta_r}. \quad (12)$$

The parameter $P(\theta)$ is the phase function for scattering:

$$P(\theta) = \frac{1 - \rho^2}{(1 + \rho^2 - 2\rho \cos \theta)^{3/2}}. \quad (13)$$

The parameter θ is the actual scattering angle at the cloud top

$$\cos \theta = \cos \theta_i \cos \theta_r - \sin \theta_i \sin \theta_r \cos(\varphi_i - \varphi_r) \quad (14)$$

where θ_i is the incident zenith angle, θ_r is the reflected zenith angle, φ_i is the incident azimuth angle, and φ_r is the reflected azimuth angle [62].

The Cox-Munk model, as developed by Charles Cox and Walter Munk, is used to calculate the emissivity and reflectivity of the sea surface. According to this model, the sea surface exhibits relative roughness due to the formation of numerous wavelets, with the slope distribution of these wavelets following specific statistical characteristics. This model computes the BRDF for

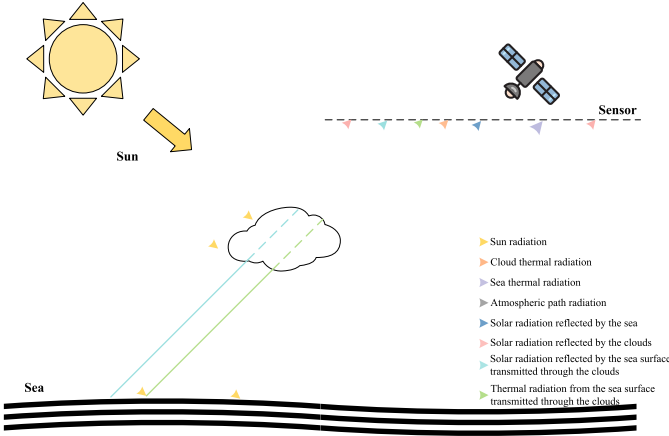


Fig. 7. Schematic diagram of radiative transfer for the cloud-sea scenario.

each wavelet surface, thus allowing for the calculation of sea surface emissivity, which is then used to determine the radiation of the sea surface [63].

C. High-Precision Calculation of Infrared Radiance for Cloud-Sea Background

To investigate the infrared radiation of the cloud-sea background received by payloads, the combined contributions of multiple radiation sources were comprehensively considered in this study. These contributions include the thermal radiation emitted by the clouds, the reflection of solar radiation by the clouds, the sea surface thermal radiation transmitted through the clouds, and the sea surface reflection of solar radiation. Furthermore, the model incorporates the impact of atmospheric path thermal radiation. This integrated analysis of multiple radiation sources ensures the completeness and accuracy of the investigation into the radiation characteristics of the cloud-sea background, as illustrated in Fig. 7.

1) *The Thermal Radiation of the Clouds:* The cloud absorbs a portion of solar radiation while emitting radiative energy due to the increase in temperature. The radiation from the cloud temperature T_{cloud} can be approximated to that of a gray body

$$L_{c,\text{self}} = \epsilon_{\text{cloud}}(\lambda) \frac{M(T_{\text{cloud}}, \lambda)}{\pi} \quad (15)$$

where $\epsilon_{\text{cloud}}(\lambda)$ is the emissivity of the cloud at wavelength λ , and $L_{c,\text{self}}$ is cloud thermal radiation.

2) *The Solar Radiation Reflected by the Clouds:* Different types of clouds contain ice and water particles of varying shapes and sizes, which can significantly scatter energy when illuminated by the sun. This can cause significant interference with target detection while operating space-based infrared detection systems. Therefore, the calculation of the solar radiation reflected by the cloud layer $L_{c,\text{refl}}$ is as follows:

$$L_{c,\text{refl}} = \tau_{s-c} L_{\text{sun}} \cos \theta_i \text{BRDF}(\lambda, \theta_i, \varphi_i, \theta_r, \varphi_r) d\omega \quad (16)$$

where τ_{s-c} is the transmittance for sensor to cloud, L_{sun} is the solar radiance.

3) *The Thermal Radiation of The Sea Surfaces.:* Radiation from the sea surface plays a critical role in infrared detection systems. When analyzing this radiation, it is important to consider the thermal radiation emitted by the sea surface and the “glitter” effect observed in the MWIR band at certain observation angles. This glitter effect is caused by the reflection of solar radiation off the sea surface. The radiation of the sea surface temperature can be calculated using

$$L_{s,\text{self}} = \epsilon_{\text{sea}}(\lambda) \frac{M(T_{\text{sea}}, \lambda)}{\pi} \quad (17)$$

where $\epsilon_{\text{sea}}(\lambda)$ is the emissivity of the sea at wavelength λ , $L_{s,\text{self}}$ is sea thermal radiation.

4) *The Solar Radiation Reflected by the Sea Surface.:*

$$L_{s,\text{refl}} = \tau_{s-s} L_{\text{sun}} \cos \theta_i \text{BRDF}(\lambda, \theta_i, \varphi_i, \theta_r, \varphi_r) d\omega \quad (18)$$

where τ_{s-s} represents the atmospheric transmittance from the detector to the sea surface, and $d\omega$ is the solid angle of the solar radiation reaching the sea surface.

5) *Atmospheric Path Radiation.:* The atmospheric path radiation $L_{\text{atm}}(\lambda)$ is calculated using the atmospheric radiation software MODTRAN.

6) *Total Radiation Calculation.:* When detecting sea-cloud scenes from a space-based platform, the total radiation in cloud-free areas is taken as a combination of the sea surface radiation, solar radiation reflected by the sea surface, and atmospheric path radiation. These components form the radiation field of the sea-cloud scene.

$$L_{\text{total}}(\lambda) = \tau_s L_s(\lambda) + L_{\text{atm}}(\lambda) \quad (19)$$

where $L_s = L_{s,\text{self}} + L_{s,\text{refl}}$.

In the presence of clouds, the radiation field is more complex, and it includes direct radiation from the clouds, solar radiation reflected by the cloud layer, radiation from the sea surface transmitted through the cloud layer, solar radiation reflected by the sea surface transmitted through the cloud layer, and atmospheric path radiation.

$$L_{\text{total}}(\lambda) = \tau_c L_c(\lambda) + \tau_s L_s(\lambda) + \tau_{sc} L_s(\lambda) + L_{\text{atm}}(\lambda) \quad (20)$$

where $L_c = L_{c,\text{self}} + L_{c,\text{refl}}$, τ_c , τ_s and τ_{sc} represent the atmospheric transmittances from the cloud top to the detector, from the sea surface to the detector, and from the sea surface through the cloud layer to the detector, respectively. These values are calculated using Modtran 5.0 software.

D. Infrared Cloud-Sea Scenario Simulation Confidence Evaluation

1) *Morphological Evaluation Analysis Based on 2-D Histograms:* To accurately assess the confidence level of simulated cloud images, we first focused on the shape distribution of the simulated clouds, as this directly impacts the realism of the simulation. The 2-D histogram visually and intuitively represents the statistical correlation or visual blur characteristics of the infrared images. Information entropy reflects the distribution of pixel values in an image; more complex images generally have higher information entropy. Thus, the richness and complexity of an image can be evaluated by using its information entropy.

The image confidence can be quantitatively analyzed using the entropy value (EV), density (Den), diagonal peak (DP), and FD. Two-dimensional histogram statistics effectively illustrate neighborhood correlation in infrared images, while considering the overall information entropy and FD. Therefore, the simulated images can be analyzed and evaluated optimally using both the graphical representation of the 2-D histogram and objective statistical data.

Let $f(x, y)$, $x \in [0, M - 1]$, $y \in [0, N - 1]$ denote a grayscale cloud image of size $M \times N$, where x and y are the horizontal and vertical coordinates of the image, respectively. Let $G_L = f(x, y)$, $G_R = f(x + 1, y)$ where G_L and G_R represent the grayscale values in the image, and W be the number of grayscale levels. The 2-D histogram represents as the count of occurrences of the adjacent pixel grayscale pairs $G(G_L, G_R)$. This histogram show the distribution of pixel values in combinations of two grayscale levels. For images with strong correlation, the 2-D histograms exhibit a higher amplitude, density, and distinct peak along the diagonal where ($G_L = G_R$) when compared with the surrounding areas.

The EV can be computed by the following equation:

$$EV = - \sum_{G_L=0}^{W-1} \sum_{G_R=0}^{W-1} Pr(G_L, G_R) \log_2 Pr(G_L, G_R) \quad (21)$$

where $Pr(G_L, G_R)$ represents the probability of a pair of pixels with gray levels G_L and G_R . Density can be defined as the average reciprocal of the number of gray levels between adjacent pixels in the entire image, representing the density or correlation of the image. The mathematical expression of Den is as follows:

$$Den = \frac{1}{(M - 1) \times N} \sum_{G_L=0}^{W-1} \sum_{G_R=0}^{W-1} \frac{1}{1 + |G_R - G_L|} G(G_L, G_R). \quad (22)$$

The DP characterizes the average height of the cross-section of the 2-D histogram along the diagonal [64]

$$DP = \frac{\sum_{G_L=0}^{W-1} G(G_L, G_L)}{W - 1}. \quad (23)$$

The statistical measures of the 2-D histogram effectively illustrate neighborhood correlations in infrared images. Analyzing and evaluating simulated images using these statistical measures provides an objective assessment. Discrepancies between the simulated and real on-orbit images were validated using the RMSE indicator in (24)

$$\begin{cases} er_{EV} = \frac{|EV_{true} - EV_{sim}|}{EV_{sim}} \\ er_{Den} = \frac{|Den_{true} - Den_{sim}|}{Den_{sim}} \\ er_{DP} = \frac{|DP_{true} - DP_{sim}|}{DP_{sim}} \\ er_{FD} = \frac{|FD_{true} - FD_{sim}|}{FD_{sim}} \\ RMSE = \sqrt{\frac{er_{EV}^2 + er_{Den}^2 + er_{DP}^2 + er_{FD}^2}{4}}. \end{cases} \quad (24)$$

2) *Radiative Simulation Accuracy Analysis Based on MODTRAN*: MODTRAN's status as the primary standard of comparison for the calculation of infrared radiative properties stems from

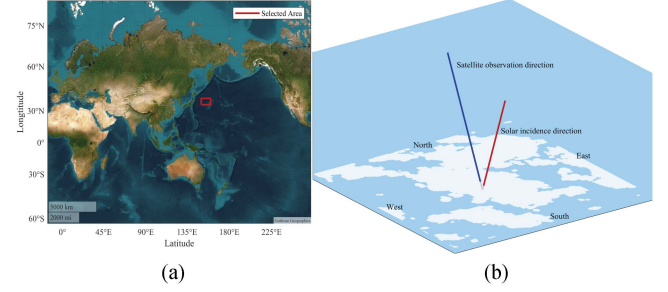


Fig. 8. Detection scenario Settings. (a) Map perspective. (b) Spatial perspective.

its excellence in accuracy, reliability, and wide range of applications. This atmospheric radiative transfer model is advanced and validated as the de facto standard in several related fields. Its comprehensive spectral coverage, detailed atmospheric modeling, and flexible parameter settings ensure its optimal suitability for infrared radiation studies [36], [41].

IV. EXPERIMENTAL RESULTS AND ANALYSIS

A. Detection Scenario Parameter Configuration

By configuring the simulation scene parameters, this aims to provide a more accurate infrared cloud-sea scenario simulation model, laying a solid foundation for subsequent tasks such as performance evaluation of infrared payload digital twin systems and target detection inversion. At 35°N , 150°E on April 20, 2019, at 12:30 PM, the solar zenith angle and azimuth angles were calculated as 24.39° and 198.72° . The reflection zenith angle was set to 20° , and the reflection azimuth angle was set to 18.72° . The atmospheric model for the simulation scenario is based on the 1976 U.S. Standard Atmosphere. The detection scenario settings are shown in Fig. 8.

The precision of infrared radiation calculations for clouds and the sea surface is closely related to the background temperature settings for both. The sea surface temperature was determined using the global sea surface temperature dataset from 2002–2019 [63], [65]. MOD08_M3, a Level-3 MODIS gridded atmospheric monthly global joint product, provides monthly $1 \times 1^\circ$ grid averages of cloud optical properties [66], which we use to set the temperature of clouds in the simulation scenario.

B. Static Infrared Cloud-Sea Scenario Simulation Results and Evaluation

Considering the detection scenarios comprehensively, the proposed method can generate infrared cloud-sea scenario images with multibands, various parameters, controllable resolution, and adjustable coverage. By integrating multiple data sources and image processing algorithms, this method provides highly flexible and accurate infrared cloud-sea images that meet practical application requirements.

1) *Static Infrared Cloud-Sea Scenario Parameters*: The initial scene settings, as shown in Table I, and have a spatial resolution of 20 m. The reflection zenith angle is varied from 0°

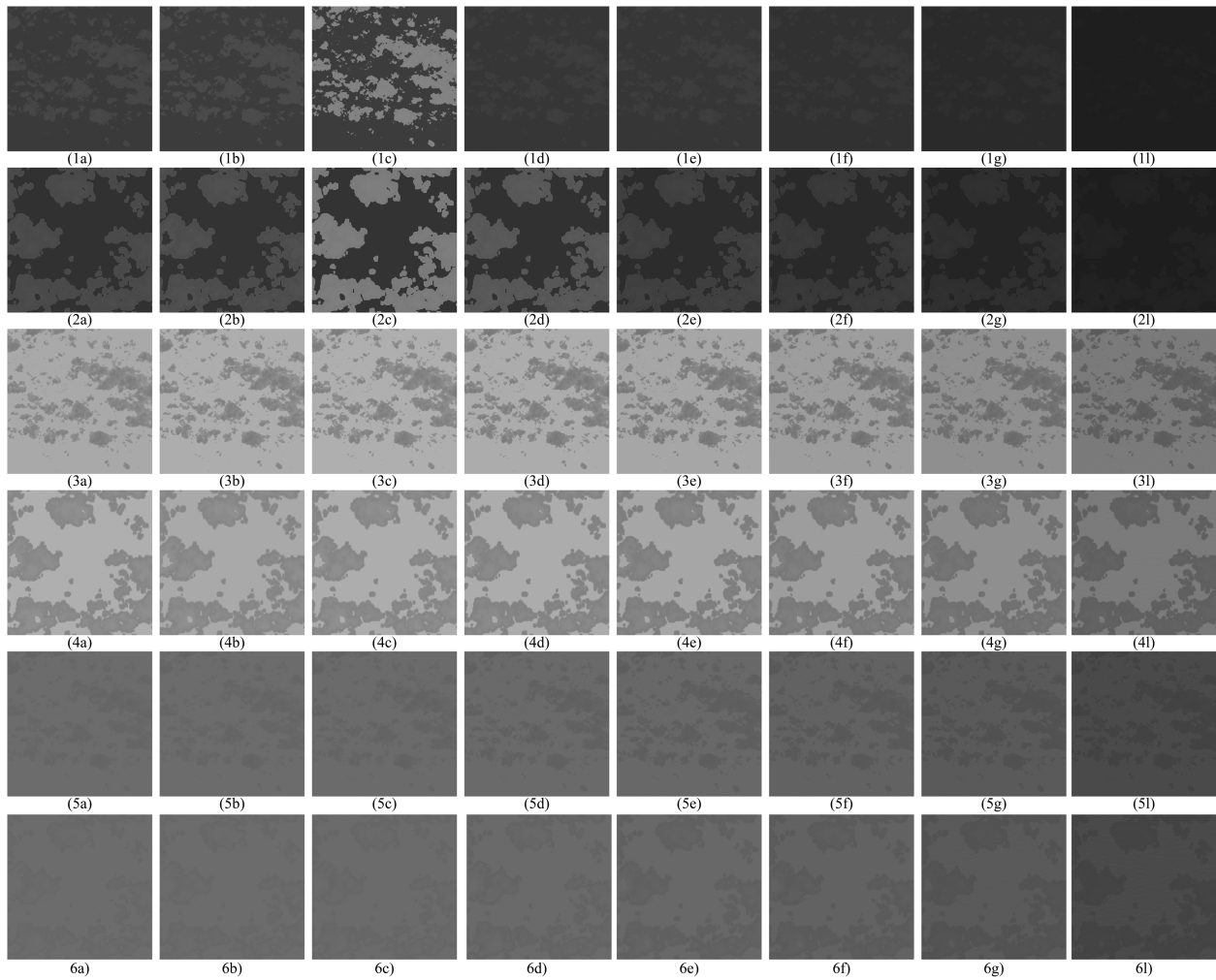


Fig. 9. Static cloud-sea scenario simulated images based on the data-driven method. (1) Scenario1, (2) Scenario2, (3) Scenario3, (4) Scenario4, (5) Scenario5, (6) Scenario6. (a) 0° . (b) 10° . (c) 20° . (d) 30° . (e) 40° . (f) 50° . (g) 60° . (h) 70° .

TABLE I
PARAMETER SETTINGS FOR STATIC CLOUD-SEA SCENARIO SIMULATION

Scenario	Cloud data	Spectral band	Coverage
Scenario1	New Technology Satellite	2.7-3.0 μm	30%
Scenario2	Qilu-2 Satellite	2.7-3.0 μm	47%
Scenario3	New Technology Satellite	3.0-5.0 μm	30%
Scenario4	Qilu-2 Satellite	3.0-5.0 μm	47%
Scenario5	New Technology Satellite	8.0-14.0 μm	30%
Scenario6	Qilu-2 Satellite	8.0-14.0 μm	47%

to 70° in steps of 10° . The simulation covers different spectral bands of the static cloud-sea scene to analyze the impact of the detection angle on the infrared cloud-sea background.

2) *Static Infrared Cloud-Sea Scenario Simulation Results:* By integrating high-quality on-orbit data from the Qilu-2 and New Technology satellites, we created a static cloud-sea background dataset, providing essential support for infrared target detection and recognition research. The simulated images of

2.7–3.0 μm , 3.0–5.0 μm , and 8.0–14.0 μm , respectively, are shown in Fig. 9.

For the scenario configurations shown in Table I, we successfully implemented multispectral infrared scene simulation of static sea clouds based on the orbital imagery data from Qilu-2 and New Technology satellites, conducting systematic verification under various detection angles. Research findings indicate that in the 2.7–3.0 μm band, the infrared images of Scenarios 1 and 2 exhibit significantly higher brightness when the reflection zenith angle is at 20° and 30° . This phenomenon can be attributed to the specular reflection effect in sea cloud scenes—when the sum of reflection and incidence angles approaches 180° , the enhanced infrared radiation energy entering the detector results in higher image brightness values. In the 3.0–5.0 μm band, the clouds display characteristic black cloud features, with thinner cloud edges manifesting as brighter peripheries and darker centers, as clearly demonstrated in Scenario 4. In the LWIR band, the thermal radiation from the sea cloud scene itself dominates, while reflected radiation is relatively weak, resulting in images with characteristically blurred edges, which closely corresponds to the features observed in orbital measurements.

TABLE II
SIMULATION RESULTS OF STATIC CLOUD-SEA RADIANCE ($W \cdot sr^{-1} \cdot m^{-2}$)

Scenario	Method	$\theta_f = 0^\circ$	$\theta_f = 10^\circ$	$\theta_f = 20^\circ$	$\theta_f = 30^\circ$	$\theta_f = 40^\circ$	$\theta_f = 50^\circ$	$\theta_f = 60^\circ$	$\theta_f = 70^\circ$
Scenario3	Ours	0.625	0.636	0.641	0.632	0.608	0.574	0.526	0.450
	Modtran	0.574	0.573	0.569	0.562	0.552	0.536	0.511	0.466
	RE	8.95%	11.04%	12.74%	12.35%	10.19%	6.99%	2.86%	3.32%
Scenario4	Ours	0.603	0.611	0.616	0.605	0.583	0.551	0.506	0.433
	Modtran	0.552	0.551	0.548	0.541	0.531	0.516	0.493	0.449
	RE	9.19%	10.90%	12.44%	11.79%	9.63%	6.69%	2.73%	3.59%
Scenario5	Ours	36.044	36.007	35.888	35.661	35.276	34.617	33.429	31.128
	Modtran	34.879	34.851	34.766	34.613	34.373	34.006	33.423	32.353
	RE	3.34%	3.32%	3.23%	3.03%	2.63%	1.80%	0.02%	3.79%
Scenario6	Ours	36.623	36.578	36.435	36.168	35.725	34.991	33.713	31.287
	Modtran	37.754	37.722	37.623	37.446	37.169	36.744	36.068	34.828
	RE	3.00%	3.03%	3.16%	3.41%	3.89%	4.77%	6.53%	10.17%

3) *Static Infrared Cloud-Sea Scenario Simulation Evaluation*: In static cloud-sea scenario simulation, we adopt a data-driven approach, utilizing real on-orbit images for simulation, and therefore do not perform morphological confidence assessment, only focus on comparing with MODTRAN radiative calculation results. In the 2.7–3.0 μm infrared band, the average radiance of the infrared images simulated by this method is 0.001–0.002 $W \cdot sr^{-1} \cdot m^{-2}$, which is consistent with the results calculated by MODTRAN. For radiative calculation results in the 3.0–5.0 μm and 8.0–14.0 μm infrared bands, shown in Table II, which validates the reliability and accuracy of this method in static cloud-sea scene simulation.

The analysis results demonstrate that in the infrared radiation assessment, within the 3.0–5.0 μm spectral band, both our proposed method and MODTRAN simulation results fall within the 0.4–0.6 $W \cdot sr^{-1} \cdot m^{-2}$, effectively validating the feasibility of our approach. In the 8.0–14.0 μm spectral band, our method shows excellent agreement with MODTRAN simulation results, particularly for reflection angles between 0–60°, where the relative error (RE) in LWIR radiation remains within 3%, fully meeting practical engineering requirements. Notably, when the reflection angle reaches 70°, both methods exhibit a significant downward trend in their calculations. This phenomenon can be attributed to the close correlation between infrared radiation and atmospheric transmittance—under large-angle conditions of 70°, atmospheric transmittance experiences a sharp decline.

C. Dynamic Infrared Cloud-Sea Scenario Simulation Results and Evaluation

1) *Dynamic Infrared Cloud-Sea Scenario Simulation Parameters*: We propose a fractal-driven dynamic cloud-sea scene simulation method that achieves high-quality scene reconstruction through iterative optimization based on the FD of on-orbit images. By comprehensively analyzing the fractal characteristics of satellite-observed marine atmospheric scenes, our approach significantly advances the fidelity and realism of dynamic cloud-sea scenario simulation, offering substantial methodological innovations for target detection and recognition in complex maritime environments.

Table III lists the parameters of the cloud fractal simulation after optimization based on the FD of the on-orbit image. Dynamic

TABLE III
CORRECTED FRACTAL CONTROL PARAMETER VALUES FOR DIFFERENT TYPES OF CLOUDS

Cloud	r	H	L	k	Cloud Height
Stratus	3	0.8	[10, 10]	0-4	0.033–1.0 Km
Cumulus	3	0.7	[30, 30]	0-7	0.066–3.0 Km
Cirrus	3	0.8	[50, 10]	0-4	6.000–10.0 Km
Simulated	4	0.8	[3, 7]	0-10	0.333–6.0 Km

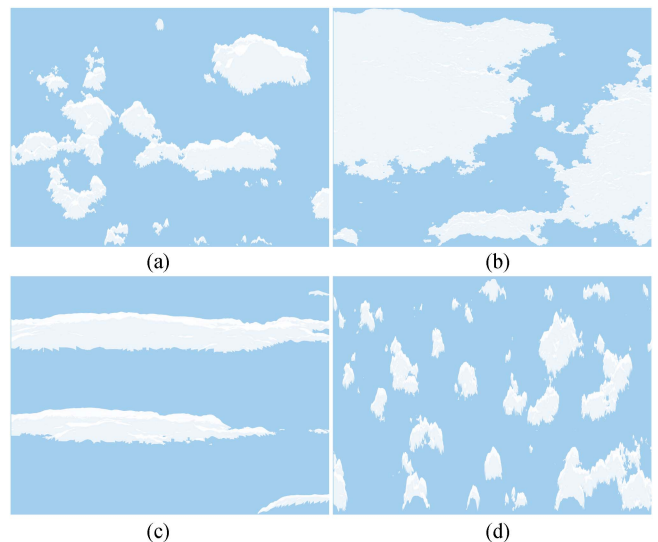


Fig. 10. Cloud-sea simulation scenarios. (a) Cumulus and sea scenario. (b) Stratocumulus and sea scenario. (c) Cirrus and sea scenario, (d) Simulated on-orbit cloud and sea scenario.

simulated cloud-sea scenarios from a space-based detection perspective is shown in Fig. 10. The resulting image, with a resolution of 20 m and dimensions of 800 × 800 pixels, simulates 3-D cloud-sea backgrounds: (a) cumulus and sea scenario, (b) stratocumulus and sea scenario, (c) cirrus and sea scenario, and (d) simulated on-orbit cloud and sea scenario. In Fig. 10, it is observed that at a wind speed of 10 m/s, corresponding to sea state 5, the maximum sea surface undulation is around 2.5 m, which aligns with the wave height of 2.5 to 4.0 m typical of sea state 5 [3], [46].

TABLE IV
SIMULATION RESULTS OF DYNAMIC CLOUD-SEA RADIANCE ($W \cdot sr^{-1} \cdot m^{-2}$)

Infrared Band	Method	$\theta_f = 0^\circ$	$\theta_f = 10^\circ$	$\theta_f = 20^\circ$	$\theta_f = 30^\circ$	$\theta_f = 40^\circ$	$\theta_f = 50^\circ$	$\theta_f = 60^\circ$	$\theta_f = 70^\circ$
2.7–3.0 μm	Ours	0.0019	0.0020	0.0025	0.0022	0.0018	0.0016	0.0013	0.0010
	Modtran	0.0019	0.0019	0.0019	0.0019	0.0018	0.0018	0.0017	0.0017
	Ours/Modtran	0.9806	1.0631	1.3344	1.1807	0.9866	0.8843	0.7748	0.6168
3.0–5.0 μm	Ours	0.616	0.626	0.632	0.622	0.599	0.565	0.519	0.444
	Modtran	0.552	0.551	0.548	0.541	0.531	0.516	0.493	0.449
	RE	11.64%	13.68%	15.37%	14.88%	12.66%	9.45%	5.26%	1.13%
8.0–14.0 μm	Ours	36.767	36.726	36.591	36.338	35.911	35.194	33.919	31.472
	Modtran	37.754	37.722	37.623	37.446	37.169	36.744	36.068	34.828
	RE	2.61%	2.64%	2.74%	2.96%	3.38%	4.22%	5.96%	9.64%

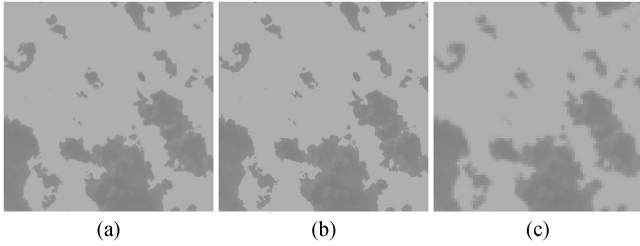


Fig. 11. Infrared cloud-sea images in different spatial resolutions. (a) 5 (m). (b) 20 (m). (c) 50 (m).

2) *Dynamic Cloud-Sea Scenario Simulation Results*: During the simulation, the satellite speed was set to 1 km/s. With a spatial resolution of 20 m for the simulated images, the image shifted 50 pixels in the x -direction with each update, while remaining unchanged in the y -direction. This method effectively simulated the push-broom imaging process of the satellite, thus ensuring that the sequence of simulated images reflected physical changes. By performing upsampling and downsampling on images, the spatial resolution can be flexibly adjusted to meet the needs of different application scenarios. Whether for rapid monitoring of large areas or detailed analysis of local regions, these techniques provide robust support. Fig. 11 shows infrared cloud-sea images with spatial resolutions of 5, 20, and 50 m. Fig. 12 presents the dynamic infrared stratus cloud-sea simulation results in (1) 2.7–3.0 μm , (2) 3.0–5.0 μm , and (3) 8.0–14.0 μm . The proposed method supports radiation calculation and image simulation in infrared multispectral bands.

Radiation measured in 3.0–5.0 μm infrared band during the daytime includes both direct solar radiation and solar radiation reflected by clouds and the sea surface. The amount of radiation received by the satellite during the daytime depends on the albedo, emissivity, and temperature of the clouds and sea surface. Higher temperatures, albedo, and emissivity result in greater radiation received by the satellite, and vice versa. In the LWIR band, the radiation from clouds and the sea surface primarily comprises their own thermal radiation, with minimal reflected solar radiation. Consequently, in the LWIR band, the radiance images of clouds and the sea surface become blurred and difficult to distinguish.

2) *Radiative Error Assessment Based on MODTRAN*: The results of cloud-sea background radiation brightness obtained

TABLE V
SIMULATION RESULTS OF INFRARED CLOUD SEA SCENES FOR DIFFERENT LOCATIONS ($W \cdot sr^{-1} \cdot m^{-2}$)

Scenario	Latitude	θ_i ($^\circ$)	φ_i ($^\circ$)	Radiance
Scenario19	35°N, 135°E	24.625	198.457	0.629
Scenario20	35°N, 145°E	23.746	186.666	0.630
Scenario21	35°N, 155°E	26.296	209.186	0.627
Scenario22	35°N, 165°E	24.652	198.429	0.629
Scenario23	35°N, 175°E	23.774	186.648	0.630
Scenario24	35°N, 185°E	26.320	209.150	0.627
Scenario25	35°N, 195°E	24.678	198.400	0.629
Scenario26	35°N, 205°E	23.802	186.630	0.630
Scenario27	35°N, 215°E	26.345	209.115	0.627
Scenario28	35°N, 225°E	24.705	198.372	0.629
Scenario29	35°S, 135°E	46.952	349.600	0.613
Scenario30	35°S, 145°E	46.435	356.302	0.614
Scenario31	35°S, 155°E	47.905	343.075	0.613
Scenario32	35°S, 165°E	46.923	349.600	0.613
Scenario33	35°S, 175°E	46.406	356.306	0.614
Scenario34	35°S, 185°E	47.876	343.071	0.613
Scenario35	35°S, 195°E	46.894	349.600	0.613
Scenario36	35°S, 205°E	46.377	356.309	0.614
Scenario37	35°S, 215°E	47.847	343.067	0.613
Scenario38	35°S, 225°E	46.865	349.600	0.613

by the proposed method and Modtran, along with the ratios or RE, for the 2.7–3.0 μm , 3.0–5.0 μm , and 8.0–14.0 μm infrared bands are shown in Table IV. The satellite side swing angle is generally within 70° and the error of this method can meet most detection requirements. The RE in the 3.0–5.0 μm infrared band is approximately 15%; whereas, the RE in the 8.0–14.0 μm infrared band is less than 10%. Therefore, this method can meet the detection requirements.

Combining the analysis of radiative data from on-orbit infrared cloud-sea images, the results revealed that the radiative in the mid-wave spectrum is approximately in the order of $10^{-1} W \cdot sr^{-1} \cdot m^{-2}$. Ignoring potential errors in the inversion process, these experimental results align with the magnitude of on-orbit measured data, thus indicating that the simulation results meet accuracy requirements.

D. Infrared Cloud-Sea Simulation Results Under Different Conditions

1) *Dynamic Cloud-Sea Scenario Simulation Across Different Seasons*: To analyze the effect of season on infrared cloud-sea scenario simulation, we simulated infrared scenes for different

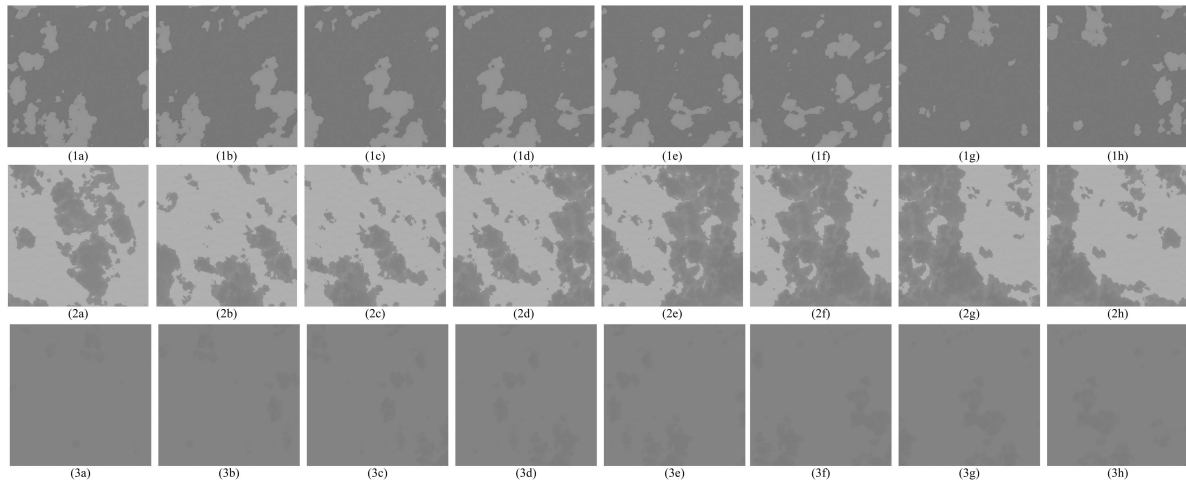


Fig. 12. Dynamic infrared stratus cloud-sea simulation results in (1) 2.7–3.0 μm , (2) 3.0–5.0 μm , and (3) 8.0–14.0 μm . (a) T=1s. (b) T=2s. (c) T=3s. (d) T=4s. (e) T=5s. (f) T=6s. (g) T=7s. (h) T=8s.

TABLE VI
SIMULATION RESULTS OF INFRARED CLOUD-SEA SCENES FOR DIFFERENT SEASONS ($\text{W} \cdot \text{sr}^{-1} \cdot \text{m}^{-2}$)

Scenario	Date	θ_i ($^\circ$)	φ_i ($^\circ$)	Radiance
Scenario7	2019.01.20	55.420	185.487	0.609
Scenario8	2019.02.20	46.285	185.507	0.610
Scenario9	2019.03.20	35.394	189.774	0.615
Scenario10	2019.04.20	24.389	198.721	0.625
Scenario11	2019.05.20	16.814	208.248	0.634
Scenario12	2019.06.20	13.131	210.129	0.639
Scenario13	2019.07.20	15.184	201.584	0.636
Scenario14	2019.08.20	23.205	196.578	0.627
Scenario15	2019.09.20	34.784	196.069	0.616
Scenario16	2019.10.20	46.415	195.409	0.610
Scenario17	2019.11.20	55.583	192.749	0.609
Scenario18	2019.12.20	58.908	188.786	0.608

months based on the parameters in Table VI. The cloud type used is the “simulated” type, as shown in Table III.

The data presented in Table VI highlighted distinct seasonal variations in the simulated radiance of infrared cloud-sea backgrounds. In winter (e.g., Scenario7 in January and Scenario18 in December), the radiance values are lower, approximately 0.609 and 0.608 $\text{W} \cdot \text{sr}^{-1} \cdot \text{m}^{-2}$, respectively. These lower values correspond to smaller solar zenith angles and reduced solar irradiance due to the Sun’s lower position in the sky during winter. In summer (e.g., Scenario12 and Scenario13 in June and July), the radiance values are higher, reaching 0.639 and 0.636 $\text{W} \cdot \text{sr}^{-1} \cdot \text{m}^{-2}$, respectively. This increase corresponds to larger solar zenith angles and more direct solar radiation during summer, leading to higher atmospheric absorption and scattering, which increase overall radiance.

Transitional seasons, such as spring (e.g., Scenario9 in March) and autumn (e.g., Scenario15 in September), show intermediate radiance values of around 0.615 and 0.616 $\text{W} \cdot \text{sr}^{-1} \cdot \text{m}^{-2}$, reflecting moderate solar zenith angles during the equinoxes. The consistent radiance variations across scenarios

highlight the significant impact of seasonal changes in solar geometry—especially solar zenith and azimuth angles—on the radiative properties of infrared cloud-sea simulations. This emphasizes the importance of accounting for seasonal effects in radiative transfer modeling and infrared payload design.

2) *Dynamic Cloud-Sea Scenario Simulation at Different Geographic Locations*: By maintaining other factors, this simulation approach was focused on mid-latitude areas, and analyzed the effect of latitude and longitude on the scenario, as shown in Table V.

Table V presents simulation parameters for various infrared cloud-sea scenes, covering latitudes, solar zenith and azimuth angles, and corresponding radiance values for different scenarios. The scenarios are organized by latitude and longitude, focusing on two main latitude bands, 35°N and 35°S, representing distinct seasonal variations in solar illumination.

The solar zenith angles for northern scenarios (35°N) range from 23.746° to 26.52°, indicating higher solar elevation, while southern scenarios (35°S) show larger angles (46.37° to 47.90°), indicating lower solar elevation. This contrast highlights seasonal variations in solar radiation. Solar azimuth angles vary between 186.63° and 356.30° representing different illumination directions vital for accurate infrared cloud-sea modeling. Radiance values remain consistent, ranging from 0.613 to 0.630 $\text{W} \cdot \text{sr}^{-1} \cdot \text{m}^{-2}$, indicating controlled atmospheric and surface conditions, which allows focused analysis of solar parameter effects on the simulated imagery.

In summary, the data in Table V provide a comprehensive framework for evaluating the influence of solar angles and geographical location on infrared radiance. These parameters support the simulation of multiscenario, multitype cloud-sea backgrounds, essential for applications such as infrared payload calibration and optoelectronic system performance assessments.

3) *Dynamic Cloud-Sea Scenario Simulation Across Different Coverage*: The cloud coverage is an important factor in infrared image target detection, as it can influence the performance of the

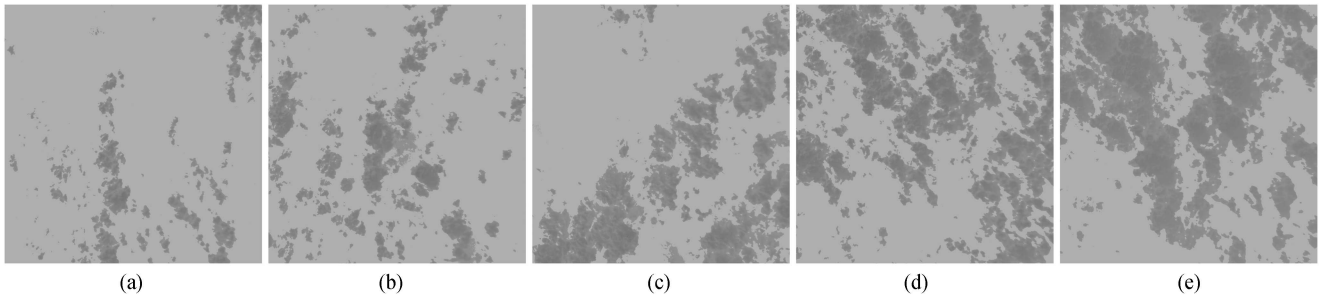


Fig. 13. Infrared cloud-sea simulation with different coverage. (a) Coverage=10%. (b) Coverage=20%. (c) Coverage=30%. (d) Coverage=40%. (e) Coverage=50%.

TABLE VII
AVERAGE RADIANCE OF SIMULATED CLOUD-SEA BACKGROUND AT
DIFFERENT CLOUD COVERAGES ($W \cdot sr^{-1} \cdot m^{-2}$)

Cloud Coverage	10%	20%	30%	40%	50%
Radiance	0.648	0.638	0.624	0.606	0.604

detection algorithm and the accuracy of the results. Clouds may block ground targets, thus influencing the usability of the image. Due to the similarity between cloud and ground features, detection may be more challenging. Fig. 13 illustrates the infrared cloud-sea simulation designed to meet detection requirements, with cloud coverage rates ranging from approximately 10% to 50%. These simulations are useful for cloud target detection in infrared remote sensing images, improving the accuracy of cloud target identification.

In the simulation of infrared cloud-sea images in the 3.0–5.0 μm infrared band shown in Table VII, under identical conditions, the average radiance of the cloud-sea background decreases from 0.648 to 0.604 $W \cdot sr^{-1} \cdot m^{-2}$ as the cloud coverage increases from 10% to 50%. This trend indicates that higher cloud coverage significantly suppresses infrared radiance intensity, consistent with the on-orbit observation of clouds appearing as “dark clouds.” This phenomenon is primarily attributed to the strong absorption characteristics of clouds in the infrared spectrum, demonstrating the high physical consistency of the simulation results. It also provides critical data support for performance evaluation of infrared electro-optical payloads and the development of algorithms in complex scenarios.

E. Morphological Evaluation of Infrared Cloud-Sea Simulations

This comparative experiment utilized several key metrics to access the similarities and differences between the simulated and real on-orbit cloud background images, as shown in Fig. 14. The black areas represent NaN values, and the lighter areas represent cloud clusters. The simulation cloud type is the “simulated” type, as shown in Table III.

The RMSE between the simulated image and the real image was 3.09%, as shown in Table VIII, which demonstrates a high level of confidence with a low degree of error. The error can be attributed to inaccuracies in simulating cloud features. The

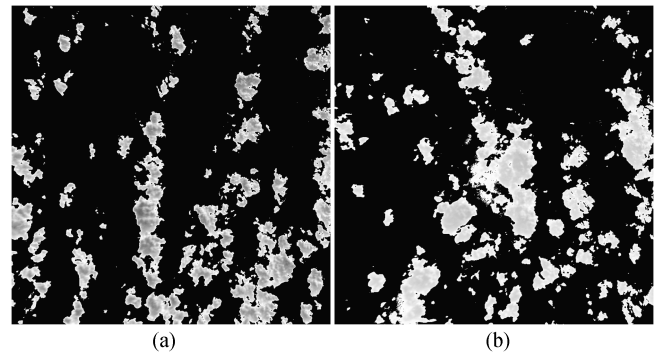


Fig. 14. Real and simulated cloud images. (a) Real cloud image. (b) Simulated cloud image.

TABLE VIII
STATISTIC COMPARISON OF REAL CLOUD IMAGE AND SIMULATED CLOUD
IMAGE

Indicators	simulated image	On-orbit image	Error(%)
<i>EV</i>	1.830	1.727	5.58%
<i>Den</i>	8.476	8.258	2.57%
<i>DP</i>	2044	2049	0.21%
<i>FD</i>	2.528	2.545	0.69%
RMSE	3.09%		

EV error was 5.58%, and reflects differences in the amount of information between the simulated and real images. Moreover, it is primarily influenced by cloud coverage and grayscale distribution. The Den error was 2.57%, which indicates the consistency of grayscale variation between the simulated and real images. The DP error was 0.21%, which indicates a high consistency in the grayscale concentration trend of local areas between the simulated and real images. The FD error was 0.69%, which describes the complexity of the image texture. A lower error suggests that the simulated image closely matches the real image in terms of texture complexity. Overall, the RMSE of 3.09% indicates a high degree of similarity between the simulated and real images.

To demonstrate the accuracy of our simulation method, we used a real image as a reference, i.e., Image1, which depicts a simulated cloud radiation scenario. In contrast, Image2 and Image3 were created using random cloud masks. The comparison is shown in Table IX. The error for the simulation

TABLE IX
STATISTIC COMPARISON OF REAL CLOUD IMAGE AND SIMULATED CLOUD
IMAGE WITH DIFFERENT COVERAGE

Indicators	Real image	Image1	Image2	Image3
Coverage	29.2%	29.2%	33.3%	20.2%
<i>EV</i>	2.267	2.267	2.547	1.843
<i>Den</i>	8.267	7.632	7.343	8.141
<i>DP</i>	1901.65	1903.27	1813.73	2031.98
<i>FD</i>	2.617	2.637	2.651	2.559
RMSE	-	4.18%	8.73%	12.01%

that matches the real image was significantly low (4.18%), whereas the errors for the random simulations were 8.73% and 12.01%. The average discrepancy of approximately 10% confirms that the simulation meets the established confidence benchmarks.

In summary, the errors in simulated image were within an acceptable range. The lower errors in density and FD indicate a high consistency with the authentic image in terms of local detail and complexity. Although there were several errors in EV and Den, the overall similarity between the simulated and real images was high, and the simulation results were considered ideal.

V. DISCUSSION

A. Variation of Radiation With Reflection Angle

This method thoroughly accounts for specular reflection in the cloud-sea environment. During specular reflection, solar radiation reflected by the cloud-sea in the absorption band initially increases and reaches its maximum radiance. As the detection angle increases, the radiance value first rises and then falls. With specular reflection, the radiance values calculated by this methods remain consistent with real cloud-sea radiance levels. The simulated images are highly aligned with real infrared cloud-sea radiance images, thus providing high confidence in their accuracy [46], [63], [67].

In radiation calculations, as can be observed from Tables II and IV, the total radiation of the cloud-sea background decreased with an increase in the reflection angle. This decrease occurred because MODTRAN models cloud-sea scenarios as diffuse reflectors, thus resulting in radiative values that remain relatively constant across different observation angles within the 0–90° range. However, the transmittance in MODTRAN is closely related to the observation angle. As the observation angle increased, the transmittance decreased until it reached 0 when the observation angle was sufficiently large to prevent the detector from illuminating the Earth’s surface (approximately 70°). This method utilizes the transmittance values calculated by MODTRAN, with radiative values changing accordingly as the observation angle increases. The transmittance from the cloud layer to the detector and from the sea surface to the detector, calculated using MODTRAN, decreases across the 0–14 μm band, as illustrated in Figs. 15 and 16. Fig. 15(a) presents the spectral transmittance varying with the reflection angle from 0–70°, and Fig. 15(b) presents the atmospheric spectral transmittance from

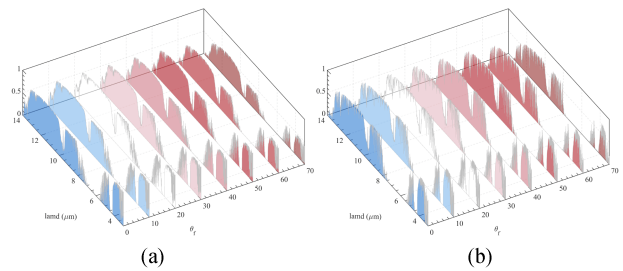


Fig. 15. Atmospheric spectral transmittance in 0-14 μm. (a) From Clouds to Detector (b) From Sea Surface to Detector.

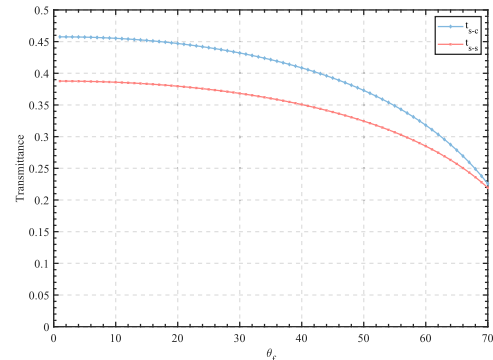


Fig. 16. Average spectral atmospheric transmittance in 0-14 μm.

the sea surface to the detector. Fig. 16 presents the average spectral atmospheric transmittance. The primary source of error between this method and MODTRAN arises from differences in transmittance.

B. Specular Reflection Phenomenon

The results in Table IV reveal that when the reflection azimuth angle was 18.72° and the reflection zenith angles were 20° and 30°, the radiance of the cloud-sea background was greater than that at other reflection zenith angles. This is because the incident solar zenith angle is set to 24.39° and the incident azimuth angle to 198.72°, which resulted in a specular reflection phenomenon, thus causing the radiance to reach its maximum. For the MWIR band, the sea surface background radiation brightness obtained by both methods was similar at small or large exit angles. However, there was a significant difference around an exit angle of 20°, with a maximum discrepancy of 15.37%. The radiation brightness simulated by this method initially increased and then decreased with the exit angle, which aligns with the results presented above; whereas, the MODTRAN simulation exhibited a continuous decrease. This suggests that the model established here can effectively capture the specular reflection phenomenon on the sea surface when exit angle and the exit direction angle are both 180°, and the incident zenith angle is close to the exit zenith angle, thus resulting in maximum radiation brightness. In contrast, the MODTRAN model approximates the sea surface as a gray body. Therefore, the model developed in this study provides a more accurate representation of specular reflection.

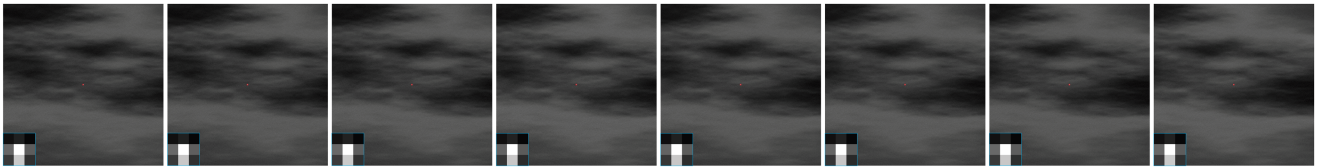


Fig. 17. Infrared degraded image.

TABLE X
COMPARISON OF THE PROPOSED METHOD, MODTRAN, AND DEEP LEARNING METHODS

Comparison Dimension	Proposed Method	MODTRAN [41]	Deep Learning [17],[18],[19],[52],[53],[54],[55]
Specular Reflection	Yes	No	Not applicable
Image Generation	Yes	No	Dataset-dependent
Data Dependency	Independent	Independent	High dependency on data
Physical Interpretability	Strong	Yes	Weak
Applicability	Wide applicability	Wide applicability	Restricted by dataset

For LWIR band, the results obtained by the two methods differed by less than 3% when the angle was under 30° . This is because the solar radiation reflected in the LWIR band is almost negligible, and the effect of specular reflection is minimal. Overall, the sea surface radiation brightness model established in this study is superior to the built-in sea surface radiation model of MODTRAN.

C. Sensitivity Analysis of Infrared Cloud-Sea Scenario Simulation

This study presents a detailed analysis of the radiative properties of the infrared cloud-sea background using our multiscenario, multiparameter simulation method. Compared to MODTRAN, which assumes a Lambertian cloud-sea background with a constant value of $0.5757 \text{ W} \cdot \text{sr}^{-1} \cdot \text{m}^{-2}$, our method shows significant sensitivity by considering factors such as geographic location, season, solar zenith and azimuth angles, and cloud coverage. The key findings are as follows:

- 1) Experimental results show that as cloud coverage increases from 10% to 50%, radiance decreases from 0.648 to $0.604 \text{ W} \cdot \text{sr}^{-1} \cdot \text{m}^{-2}$. In contrast to the fixed value in MODTRAN, our results exhibit greater sensitivity to the suppressive effect of increased cloud coverage on infrared radiation.
- 2) Results from Table VI indicate significant seasonal variations in radiance, with values ranging from 0.608 to $0.639 \text{ W} \cdot \text{sr}^{-1} \cdot \text{m}^{-2}$ in scenarios from Scenario7 to Scenario18. Summer scenarios (e.g., Scenario12 and Scenario13) show notably higher radiance compared to winter scenarios (e.g., Scenario7 and Scenario8). This highlights our method's advantage in capturing seasonal solar radiation variations, a feature not accounted for in MODTRAN's Lambertian model.
- 3) Data from Table V show that radiance values change with latitude and longitude due to solar zenith and azimuth angles. In Scenario19 and 38, radiance ranges from 0.613 to $0.630 \text{ W} \cdot \text{sr}^{-1} \cdot \text{m}^{-2}$. These variations, simplified by

MODTRAN, are better captured by our method, which accounts for geographic influences.

- 4) Our method captures the interactions between multiple parameters, including geographic location, cloud coverage, and season. For example, in Scenarios 19 and 38, radiance varies slightly despite the same latitude, due to longitude differences. This shows our model's ability to capture subtle geographic interactions.

By incorporating multiparameter simulations, our method overcomes the limitations of MODTRAN's Lambertian assumption, enhancing simulation sensitivity and physical consistency. The approach captures the effects of environmental factors on infrared radiative properties, providing higher precision for infrared payload evaluation and complex scenario analysis.

D. Support the Input of Digital Twins

Based on the simulation experiment, a convolution with the on-orbit image blur kernel combined with the addition of on-orbit image noise using target simulation technology resulted in a degraded infrared image, as shown in Fig. 17. The wavelength range is $2.7\text{--}3.0 \mu\text{m}$, the cloud type is cirrus, and the coverage rate is 100%. Such simulated images can be used for the development and testing of infrared target detection algorithms. By simulating various environments and scenarios, these images can assess the robustness of the algorithms under various conditions. Future research will focus on adjusting the algorithm to achieve various cloud effects, simulating dynamic cloud behavior, and applying fast and efficient volume rendering techniques. These areas will require further in-depth study and discussion in future research.

E. Advantages and Comparative Analysis of the Proposed Method

Our method offers the following key advantages, as shown in Table X. Unlike traditional MODTRAN methods, our approach includes specular reflection, enabling more accurate simulation of infrared cloud-sea background radiative characteristics. It

generates 2-D radiative images, rather than single-point or 1-D values, offering a more comprehensive representation of infrared radiation. Unlike deep learning methods, our approach does not depend on large datasets, avoiding limitations related to data availability or bias. Based on physical models, our method offers strong interpretability and theoretical grounding, ensuring result reliability and verifiability.

VI. CONCLUSION

In this article, we proposed a HCSS method for generating infrared radiation images, thus serving as inputs for infrared digital payloads and supporting future target detection tasks. Unlike methods that rely on on-orbit image datasets, our approach enables the generation of large-scale cloud-sea images under variable conditions. This method supports the creation of multispectral infrared radiation images across typical infrared bands, including the bands ranging from 2.7–3.0, 3.0–5.0, and 8–14 μm . The generated images feature adjustable spatial resolutions ranging from 20 to 100 m and flexible cloud coverage rates from 10% to 50%, catering to various precision and environmental requirements. Validation through comparisons with MODTRAN software and real infrared images shows high confidence in our simulated images. The average RMSE for morphological accuracy is approximately 8.3%. For radiance assessments, the simulated radiance in the 2.7–3.0 μm band aligns closely with MODTRAN calculations. In the 3.0–5.0 μm band, the RMSE is about 12.3% when the reflection angles under 60°. In the 8.0–14.0 μm band, the RMSE is less than 3.7%, thus confirming the accuracy and reliability of the proposed method. Future research will involve refining infrared cloud types and expand the database for more comprehensive cloud-sea simulations.

REFERENCES

- [1] W. Liu, M. Wu, G. Wan, and M. Xu, "Digital twin of space environment: Development, challenges, applications, and future outlook," *Remote Sens.*, vol. 16, no. 16, 2024, doi: [10.3390/rs16163023](https://doi.org/10.3390/rs16163023).
- [2] Z. Li, H. Shen, H. Li, G. Xia, P. Gamba, and L. Zhang, "Multi-feature combined cloud and cloud shadow detection in GaoFen-1 wide field of view imagery," *Remote Sens. Environ.*, vol. 191, pp. 342–358, Mar. 2017, doi: [10.1016/j.rse.2017.01.026](https://doi.org/10.1016/j.rse.2017.01.026).
- [3] W. J. Pierson Jr and L. Moskowitz, "A proposed spectral form for fully developed wind seas based on the similarity theory of SA Kitaigorodskii," *J. Geophys. Res.*, vol. 69, no. 24, pp. 5181–5190, 1964, doi: [10.1029/JZ069i024p05181](https://doi.org/10.1029/JZ069i024p05181).
- [4] K. Hasselmann et al., "Measurements of wind-wave growth and swell decay during the Joint North Sea Wave Project (JONSWAP)," *Deutsches Hydrographisches Inst.*, vol. 8, pp. 1–95, Jan. 1973.
- [5] A. Arakawa and V. R. Lamb, "A potential entropy and energy conserving scheme for the shallow water equations," *Mon. Weather Rev.*, vol. 109, no. 1, pp. 18–36, 1981, doi: [10.1175/1520-0493\(1981\)109<0018:APEAEC>2.0.CO;2](https://doi.org/10.1175/1520-0493(1981)109<0018:APEAEC>2.0.CO;2).
- [6] D. J. T. Carter, "Prediction of wave height and period for a constant wind velocity using the JONSWAP results," *Ocean Eng.*, vol. 9, no. 1, pp. 17–33, 1982, doi: [10.1016/0029-8018\(82\)90042-7](https://doi.org/10.1016/0029-8018(82)90042-7).
- [7] M. N. Zamri and M. S. Sunar, "Atmospheric cloud modeling methods in computer graphics: A review, trends, taxonomy, and future directions," *J. King Saud Univ.—Comput. Inf. Sci.*, vol. 34, no. 6, Part B, pp. 3468–3488, 2022, doi: [10.1016/j.jksuci.2020.11.030](https://doi.org/10.1016/j.jksuci.2020.11.030).
- [8] I. Wilf and Y. Manor, "Simulation of sea surface images in the infrared," *Appl. Opt.*, vol. 23, no. 18, pp. 3174–3180, Sep., 1984, doi: [10.1364/AO.23.003174](https://doi.org/10.1364/AO.23.003174).
- [9] S. N. Lashansky, N. Ben-Yosef, and A. Weitz, "Simulation of ground-based infrared cloudy sky images," *Opt. Eng.*, vol. 32, no. 6, pp. 1290–1297, 1993.
- [10] A. Benassi, F. Szczap, A. Davis, M. Masbou, C. Cornet, and P. Bleuyard, "Thermal radiative fluxes through inhomogeneous cloud fields: A sensitivity study using a new stochastic cloud generator," *Atmospheric Res.*, vol. 72, no. 1–4, pp. 291–315, 2004, doi: [10.1016/j.atmosres.2004.03.018](https://doi.org/10.1016/j.atmosres.2004.03.018).
- [11] C. Cornet, L. C-Labonnote, and F. Szczap, "Three-dimensional polarized Monte Carlo atmospheric radiative transfer model (3DMCPOL): 3D effects on polarized visible reflectances of a cirrus cloud," *J. Quant. Spectrosc. Radiat. Transf.*, vol. 111, no. 1, pp. 174–186, 2010, doi: [10.1016/j.jqsrt.2009.06.013](https://doi.org/10.1016/j.jqsrt.2009.06.013).
- [12] S. He, X. Wang, R. Xia, W. Jin, and J. Liang, "Polarimetric infrared imaging simulation of a synthetic sea surface with mie scattering," *Appl. Opt.*, vol. 57, no. 7, pp. B150–B159, Mar. 2018, doi: [10.1364/AO.57.00B150](https://doi.org/10.1364/AO.57.00B150).
- [13] H. Yuan, X. Wang, B. Guo, K. Li, and W. Zhang, "Modeling of e mid-wave infrared radiation characteristics of the sea surface based on measured data," *Infrared Phys. Technol.*, vol. 93, pp. 1–8, Sep. 2018, doi: [10.1016/j.infrared.2018.07.005](https://doi.org/10.1016/j.infrared.2018.07.005).
- [14] Y. Jiang, Y. Liu, Q. Peng, F. Jie, and D. Ming, "Infrared image generation method based on visible light remote sensing image," in *Proc. IEEE 3rd Adv. Inf. Manage. Commun. Electron. Autom. Control Conf.*, 2019, pp. 63–68, doi: [10.1109/imccc46724.2019.8984157](https://doi.org/10.1109/imccc46724.2019.8984157).
- [15] J. M. Jurado, E. J. Padrón, J. R. Jiménez, and L. Ortega, "An out-of-core method for GPU image mapping on large 3D scenarios of the real world," *Future Gener. Comput. Syst.*, vol. 134, pp. 66–77, Sep. 2022, doi: [10.1016/j.future.2022.03.022](https://doi.org/10.1016/j.future.2022.03.022).
- [16] A. Upadhyay, M. sharma, P. Mukherjee, A. Singhal, and B. Lall, "A comprehensive survey on synthetic infrared image synthesis," Aug. 14, 2024. Accessed: Nov. 18, 2024. [Online]. Available: <http://arxiv.org/abs/2408.06868>
- [17] R. Abbott, N. M. Robertson, J. Martinez del Rincon, and B. Connor, "Unsupervised object detection via LWIR/RGB translation," in *Proc. IEEE/CVF Conf. Comput. Vis. Pattern Recognit. Workshops*, 2020, pp. 90–91, doi: [10.1109/cvprw50498.2020.00053](https://doi.org/10.1109/cvprw50498.2020.00053).
- [18] L. Zhang, A. Gonzalez-Garcia, J. van de Weijer, M. Danelljan, and F. S. Khan, "Synthetic data generation for end-to-end thermal infrared tracking," *IEEE Trans. Image Process.*, vol. 28, no. 4, pp. 1837–1850, Apr. 2019, doi: [10.1109/TIP.2018.2879249](https://doi.org/10.1109/TIP.2018.2879249).
- [19] X. Qian, M. Zhang, and F. Zhang, "Sparse GANs for thermal infrared image generation from optical image," *IEEE Access*, vol. 8, pp. 180124–180132, 2020, doi: [10.1109/access.2020.3024576](https://doi.org/10.1109/access.2020.3024576).
- [20] K. N. Liou, Y. Takano, A. Liu, P. Yang, Q. Fu, and D. Winker, "Remote sensing of three-dimensional inhomogeneous cirrus clouds using satellite and mm-wave cloud radar data," *Geophys. Res. Lett.*, vol. 29, no. 9, pp. 741–744, 2002, doi: [10.1029/2002GL014846](https://doi.org/10.1029/2002GL014846).
- [21] R. Dulski, T. Sosnowski, and H. Polakowski, "A method for modelling IR images of sky and clouds," *Infrared Phys. Technol.*, vol. 54, no. 2, pp. 53–60, 2011, doi: [10.1016/j.infrared.2010.12.011](https://doi.org/10.1016/j.infrared.2010.12.011).
- [22] Y. Dobashi, K. Iwasaki, Y. Yue, and T. Nishita, "Visual simulation of clouds," *Vis. Inf.*, vol. 1, no. 1, pp. 1–8, 2017, doi: [10.1016/j.visinf.2017.01.001](https://doi.org/10.1016/j.visinf.2017.01.001).
- [23] N. Rimensberger, M. Gross, and T. Günther, "Visualization of clouds and atmospheric air flows," *IEEE Comput. Graph. Appl.*, vol. 39, no. 1, pp. 12–25, Jan./Feb. 2019, doi: [10.1109/MCG.2018.2880821](https://doi.org/10.1109/MCG.2018.2880821).
- [24] Y. Chen, J. Chen, and W. Huang, "3D cumulus cloud scene modelling and shadow analysis method based on ground-based sky images," *Int. J. Appl. Earth Observ. Geoinf.*, vol. 109, May 2022, Art. no. 102765, doi: [10.1016/j.jag.2022.102765](https://doi.org/10.1016/j.jag.2022.102765).
- [25] Z. Zhang, Y. Cen, F. Zhang, and X. Liang, "Cumulus cloud modeling from images based on VAE-GAN," *Vis. Res. Interact. Hum.*, vol. 3, no. 2, pp. 171–181, Apr. 2021, doi: [10.1016/j.vrih.2020.12.004](https://doi.org/10.1016/j.vrih.2020.12.004).
- [26] J. Lian, S. Wu, S. Huang, and Q. Zhao, "A novel sequence-to-sequence based deep learning model for satellite cloud image time series prediction," *Atmos. Res.*, vol. 306, Aug. 2024, Art. no. 107457, doi: [10.1016/j.atmosres.2024.107457](https://doi.org/10.1016/j.atmosres.2024.107457).
- [27] J. T. Kajiya and B. P. Von Herzen, "Ray tracing volume densities," *SIGGRAPH Comput. Graph.*, vol. 18, no. 3, pp. 165–174, Jan. 1984, doi: [10.1145/964965.808594](https://doi.org/10.1145/964965.808594).
- [28] Y. Dobashi, K. Kusumoto, T. Nishita, and T. Yamamoto, "Feedback control of cumuliform cloud formation based on computational fluid dynamics," *ACM Trans. Graph.*, vol. 27, no. 3, pp. 1–8, 2008, doi: [10.1145/1360612.1360693](https://doi.org/10.1145/1360612.1360693).
- [29] H. Qiu, L. Chen, G. Qiu, and H. Yang, "Realistic simulation of 3D cloud," *WSEAS Trans. Comput.*, vol. 12, no. 8, pp. 331–340, 2013.

- [30] F. Szczap et al., "A flexible three-dimensional stratocumulus, cumulus and cirrus cloud generator (3DCLOUD) based on drastically simplified atmospheric equations and the Fourier transform framework," *Geosci. Model Dev.*, vol. 7, no. 4, pp. 1779–1801, 2014, doi: [10.5194/gmd-7-1779-2014](https://doi.org/10.5194/gmd-7-1779-2014).
- [31] B. A. Raut et al., "Optimizing cloud motion estimation on the edge with phase correlation and optical flow," *Atmospheric Meas. Tech.*, vol. 16, no. 5, pp. 1195–1209, 2023, doi: [10.5194/amt-16-1195-2023](https://doi.org/10.5194/amt-16-1195-2023).
- [32] S. Lovejoy and D. Schertzer, "Multifractals, cloud radiances and rain," *J. Hydrol.*, vol. 322, no. 1, pp. 59–88, May, 2006, doi: [10.1016/j.jhydrol.2005.02.042](https://doi.org/10.1016/j.jhydrol.2005.02.042).
- [33] A. M. Schinder et al., "Deterministic global 3D fractal cloud model for synthetic scene generation," *Remote Sens.*, vol. 16, no. 9, Jan. 2024, Art. no. 9, doi: [10.3390/rs16091622](https://doi.org/10.3390/rs16091622).
- [34] A. Webanck, Y. Cortial, E. Guérin, and E. Galin, "Procedural cloudscapes," *Comput. Graph. Forum*, vol. 37, no. 2, pp. 431–442, 2018, doi: [10.1111/cgf.13373](https://doi.org/10.1111/cgf.13373).
- [35] G. M. Lohmann, A. Hammer, A. H. Monahan, T. Schmidt, and D. Heinemann, "Simulating clear-sky index increment correlations under mixed sky conditions using a fractal cloud model," *Sol. Energy*, vol. 150, pp. 255–264, Jul. 2017, doi: [10.1016/j.solener.2017.04.048](https://doi.org/10.1016/j.solener.2017.04.048).
- [36] R. Isaacs, W.-C. Wang, R. Worsham, and S. Goldenberg, "Multiple scattering LOWTRAN and FASCODE models," *Appl. Opt.*, vol. 26, no. 7, pp. 1272–1281, 1987, doi: [10.1364/AO.26.001272](https://doi.org/10.1364/AO.26.001272).
- [37] V. Payan and A. Royer, "Analysis of temperature emissivity separation (TES) algorithm applicability and sensitivity," *Int. J. Remote Sens.*, vol. 25, no. 1, pp. 15–37, 2004, doi: [10.1080/0143116031000115274](https://doi.org/10.1080/0143116031000115274).
- [38] S. A. Buehler, J. Mendrok, P. Eriksson, A. Perrin, R. Larsson, and O. Lemke, "ARTS, the atmospheric radiative transfer simulator—version 2.2," *Geosci. Model Dev.*, vol. 11, no. 4, pp. 1537–1556, 2018, doi: [10.5194/gmd-11-1537-2018](https://doi.org/10.5194/gmd-11-1537-2018).
- [39] K. Stammes, S.-C. Tsay, W. Wiscombe, and I. Laszlo, "DISORT, a general-purpose FORTRAN program for discrete-ordinate-method radiative transfer in scattering and emitting layered media: Documentation of methodology," NASA Goddard Space Flight Center, MD, USA, Disort Rep. Version 1.1, Mar. 2000.
- [40] R. Saunders et al., "An update on the RTTOV fast radiative transfer model (currently at version 12)," *Geosci. Model Dev.*, vol. 11, no. 7, pp. 2717–2737, 2018, doi: [10.5194/gmd-11-2717-2018](https://doi.org/10.5194/gmd-11-2717-2018).
- [41] A. Berk et al., "MODTRAN cloud and multiple scattering upgrades with application to AVIRIS," *Remote Sens. Environ.*, vol. 65, no. 3, pp. 367–375, 1998, doi: [10.1016/S0034-4257\(98\)00045-5](https://doi.org/10.1016/S0034-4257(98)00045-5).
- [42] J. S. Watson et al., "IRMA multisensor predictive signature model," in *Targets and Backgrounds: Characterization and Representation IV*. Bellingham, WA, USA: SPIE, 1998, pp. 78–92, doi: [10.1117/12.327143](https://doi.org/10.1117/12.327143).
- [43] B. A. Sieglinger, M. T. Finch, and V. T. Franques, "Sensor effects simulation for synthetic signature modeling using the strategic scene workstation," *Proc. SPIE*, vol. 1689, Sep. 1992, pp. 319–337, doi: [10.1117/12.137963](https://doi.org/10.1117/12.137963).
- [44] J. M. Cathcart, V. B. Sylvester, J. M. Baden, M. N. Cohen, G. K. Williams, and S. L. Robertson, "Multispectral signature modeling," in *Automatic Object Recognition II*. Bellingham, WA, USA: SPIE, 1992, pp. 296–304, doi: [10.1117/12.138293](https://doi.org/10.1117/12.138293).
- [45] X. Yang, H. Zhang, and S. Liao, "Infrared image simulation technology based on Vega Prime," in *Proc. Int. Conf. Image Process. Intell. Control*, SPIE, 2021, pp. 114–123, doi: [10.1117/12.2611383](https://doi.org/10.1117/12.2611383).
- [46] A. Kirk, M. Cowan, and R. D. Allen, "CAMEO-SIM: an ocean model extension to the physically accurate broadband EO scene generation system for the assessment of target vehicles within their natural environments," in *Targets and Backgrounds X: Characterization and Representation*. Bellingham, WA, USA: SPIE, 2004, pp. 288–299, doi: [10.1117/12.541303](https://doi.org/10.1117/12.541303).
- [47] A. Le Goff, J. Latger, and T. Cathala, "Evolution of SE-Workbench-EO to generate synthetic EO/IR image data sets for machine learning," in *Automatic Target Recognition XXXII*. Bellingham, WA, USA: SPIE, 2022, pp. 188–209, doi: [10.1117/12.2632231](https://doi.org/10.1117/12.2632231).
- [48] N. Li, Z. Lv, S. Wang, G. Gong, and L. Ren, "A real-time infrared radiation imaging simulation method of aircraft skin with aerodynamic heating effect," *Infrared Phys. Technol.*, vol. 71, pp. 533–541, 2015, doi: [10.1016/j.infrared.2015.06.014](https://doi.org/10.1016/j.infrared.2015.06.014).
- [49] J. Qi et al., "LESS: Large-Scale remote sensing data and image simulation framework over heterogeneous 3D scenes," *Remote Sens. Environ.*, vol. 221, pp. 695–706, Feb. 2019, doi: [10.1016/j.rse.2018.11.036](https://doi.org/10.1016/j.rse.2018.11.036).
- [50] H. Zhijian, H. Bingwei, and S. Shujin, "An infrared sequence image generating method for target detection and tracking," *Front. Comput. Neurosci.*, vol. 16, Jul. 2022, Art. no. 930827, doi: [10.3389/fncom.2022.930827](https://doi.org/10.3389/fncom.2022.930827).
- [51] T. Zhao et al., "Artificial intelligence for geoscience: Progress, challenges, and perspectives," *Innov.*, vol. 5, no. 5, 2024, Art. no. 100691, doi: [10.1016/j.xinn.2024.100691](https://doi.org/10.1016/j.xinn.2024.100691).
- [52] V. V. Kniaz, V. A. Knyaz, J. Hlad vka, W. G. Kropatsch, and V. Mizginov, *ThermalGAN: Multimodal Color-to-Thermal Image Translation for Person Re-Identification in Multispectral Dataset*. Berlin, Germany: Springer, 2019, pp. 606–624, doi: [10.1007/978-3-030-11024-6_46](https://doi.org/10.1007/978-3-030-11024-6_46).
- [53] M. A. Özkanoglu and S. Ozer, "InfraGAN: A GAN architecture to transfer visible images to infrared Domain," *Pattern Recognit. Lett.*, vol. 155, pp. 69–76, Mar. 2022, doi: [10.1016/j.patrec.2022.01.026](https://doi.org/10.1016/j.patrec.2022.01.026).
- [54] Y. Li, Y. Ko, and W. Lee, "A feasibility study on translation of RGB images to thermal images: Development of a machine learning algorithm," *SN Comput. Sci.*, vol. 4, no. 5, Jul. 2023, Art. no. 555, doi: [10.1007/s42979-023-02040-4](https://doi.org/10.1007/s42979-023-02040-4).
- [55] R. Zhang, C. Mu, M. Xu, L. Xu, Q. Shi, and J. Wang, "Synthetic IR image refinement using adversarial learning with bidirectional mappings," *IEEE Access*, vol. 7, pp. 153734–153750, 2019, doi: [10.1109/access.2019.2947657](https://doi.org/10.1109/access.2019.2947657).
- [56] D. Saupe, "Point evaluation of multi-variable random fractals," in *Visualisierung in Mathematik Und Naturwissenschaften: Bremer Computergraphik-Tage 1988*, H. Jürgens and D. Saupe, Eds. Springer:Berlin, Germany, 1989, pp. 114–126.
- [57] B. B. Mandelbrot, "The fractal geometry of nature," in *Einaudi Paperbacks*. New York, NY, USA: Henry Holt and Company, 1983. [Online]. Available: <https://books.google.com/books?id=0R2LkE3N7-oC>.
- [58] L. S. Liebovitch and T. Toth, "A fast algorithm to determine fractal dimensions by box counting," *Phys. Lett. A*, vol. 141, no. 8, pp. 386–390, Nov. 1989, doi: [10.1016/0375-9601\(89\)90854-2](https://doi.org/10.1016/0375-9601(89)90854-2).
- [59] P. Yang and K. Meyer, "Satellites and satellite remote sensing|remote sensing: Cloud properties," in *Reference Module in Earth Systems and Environmental Sciences*. New York, NY, USA: Elsevier, 2024, doi: [10.1016/B978-0-323-96026-7.00009-6](https://doi.org/10.1016/B978-0-323-96026-7.00009-6).
- [60] L. xingrun, L. Xia, M. Jing, and L. Hao, "Computation and comparison of cloud infrared radiation characteristics," *Procedia Comput. Sci.*, vol. 174, pp. 689–693, 2020, doi: [10.1016/j.procs.2020.06.143](https://doi.org/10.1016/j.procs.2020.06.143).
- [61] M. Nieto-Vesperinas, "2 - fundamentals of mie scattering," in *Dielectric Metamaterials*, I. Brener, S. Liu, I. Staude, J. Valentine, and C. Holloway, Eds. Sawston, U.K.: Woodhead Publishing, 2020, pp. 39–72, doi: [10.1016/B978-0-08-102403-4.00007-4](https://doi.org/10.1016/B978-0-08-102403-4.00007-4).
- [62] C. A. Gueymard and M. Kocifaj, "Clear-sky spectral radiance modeling under variable aerosol conditions," *Renew. Sustain. Energy Rev.*, vol. 168, 2022, Art. no. 112901, doi: [10.1016/j.rser.2022.112901](https://doi.org/10.1016/j.rser.2022.112901).
- [63] C.-A. Guérin, V. Capelle, and J.-M. Hartmann, "Revisiting the Cox and Munk wave-slope statistics using IASI observations of the sea surface," *Remote Sens. Environ.*, vol. 288, 2023, Art. no. 113508, doi: [10.1016/j.rse.2023.113508](https://doi.org/10.1016/j.rse.2023.113508).
- [64] Z. Shuli Lou Xiaodong, "IR simulated image assessment based on histogram analysis(in Chinese)," *Laser & Infrared*, vol. 41, no. 11, 2011, Art. no. 1273.
- [65] M. Cao et al., "A new global gridded sea surface temperature data product based on multisource data," *Earth Syst. Sci. Data*, vol. 13, no. 5, pp. 2111–2134, 2021, doi: [10.5194/essd-13-2111-2021](https://doi.org/10.5194/essd-13-2111-2021).
- [66] S. Platnick et al., "MODIS atmosphere L3 monthly product," in *NASA MODIS Adaptive Processing System*. Goddard Space Flight Center, USA, 2015. [Online]. Available: http://dx.doi.org/10.5067/MODIS/MOD08_M3.006.
- [67] C. Cox and W. Munk, "Measurement of the roughness of the sea surface from photographs of the Sun's glitter," *J. Opt. Soc. Amer.*, vol. 44, no. 11, pp. 838–850, Nov. 1954, doi: [10.1364/JOSA.44.000838](https://doi.org/10.1364/JOSA.44.000838).



Wen Sun received the B.S. degree in electrical and information engineering from Shanghai Maritime University, Shanghai, China, in 2021. She is currently working toward the Ph.D. degree in electronic circuit and system with Shanghai Institute of Technical Physics of the Chinese Academy of Sciences, Beijing, China.

Her research interests include infrared system modeling and simulation and image processing.



Yejin Li received the B.S. degree in information engineering from Xi'an Jiaotong University, Xi'an, China, in 2011, the M.S. degree in electrical and computer engineering from Worcester Polytechnic Institute, Worcester, MA, USA, in 2014, and the Ph.D. degree in fluid mechanics from Fudan University, Shanghai, China in 2023.

He is currently with the Shanghai Institute of Technical Physics, Chinese Academy of Sciences, Shanghai, China. His research interests include system modeling and simulation and infrared target detection.



Guangsen Liu received the B.S. degree in optoelectronic information science and engineering from Dalian University of Technology, Dalian, China, in 2020. He is currently working toward the Ph.D. degree in physical electronics with Shanghai Institute of Technical Physics, Chinese Academy of Sciences, Shanghai, China.

His research interests include radiative transfer, polarization image processing, and multimodality image fusion.



Fenghong Li received the B.S. degree in electrical and information engineering from Ocean University of China, Qingdao, China, in 2021. She is currently working toward the Ph.D. degree in circuits and systems with Shanghai Institute of Technical Physics, Chinese Academy of Sciences, Beijing, China.

Her research interests include image processing, deep learning and infrared target detection.



Peng Rao (Member, IEEE) received the B.S. degree in optoelectronic engineering from Huazhong University of Science and Technology, Wuhan, China, in 2000 and the M.S. and Ph.D. degrees in photoelectric detection system from University of Chinese Academy of Sciences, Beijing, China, in 2008 and 2014, respectively.

He is a Professor with Shanghai Institute of Technical Physics, Chinese Academy of Sciences, China. His research interests include photoelectric detection system and image processing.